https://doi.org/10.5194/egusphere-2026-2867
Preprint. Discussion started: 3 June 2026

Evaluation of sub-daily precipitation variability and its diurnal characteristics in satellite and reanalysis datasets against ground-based observations

Gyuyeon Choi[1], Eunkyo Seo[1,2], Paul A. Dirmeyer[2]

[1]Department of Environmental Atmospheric Sciences, Pukyong National University, Busan, 48513, Republic of Korea
[2]Center for Ocean-Land-Atmosphere Studies, George Mason University, Fairfax, Virginia, 22030, United States

Correspondence to: Eunkyo Seo (eseo@pknu.ac.kr)

Abstract. The diurnal cycle of precipitation serves as a fundamental diagnostic of the climate system's energy budget and hydrological cycle. Yet comprehensive evaluations of both its regular diurnal and irregular intermittent components across multiple satellite and reanalysis products against extensive ground-based observations remain limited. This study evaluates the boreal summer diurnal cycle across five satellite products and four reanalysis datasets against 6,824 ground-based stations over the Northern Hemisphere land regions, complemented by inter-product comparison over global ocean and Southern Hemisphere domains where dense sub-daily gauge networks are unavailable. This study combines sub-daily variance decomposition and harmonic analysis with atmospheric moisture budget diagnosis across contrasting precipitation regimes. Ground-based observations indicate sub-daily fluctuations account for 66.3% of total precipitation variance, with the irregular component dominating over the repeatable diurnal signal, a fraction that all evaluated datasets systematically underestimate. Satellite products reproduce the observed late-afternoon precipitation maximum with a systematic phase lag of 1–2 hours, attributable to passive microwave detection of upper-tropospheric ice-scattering signals rather than surface precipitation, while sub-daily variance fidelity differs substantially among products depending on calibration methodology. Reanalysis datasets exhibit a more severe premature phase lead of 3–6 hours over land, driven exclusively by premature convective triggering. Among reanalysis datasets, JRA-3Q shows the smallest phase difference owing to its DCAPE-based convective trigger, while NARR achieves superior performance over North America through direct assimilation of precipitation observations. Among satellite products, CMORPH shows the closest agreement with observations, as its morphing-based propagation of passive microwave retrievals preserves precipitation timing while its PDF-based bias correction maintains sub-daily temporal structure. These findings provide practical guidance for dataset selection and offer actionable physical insights for improving convective parameterization schemes and satellite retrieval algorithms.

https://doi.org/10.5194/egusphere-2026-2867
Preprint. Discussion started: 3 June 2026

1 Introduction

Precipitation serves as the primary atmospheric engine of the global water cycle, acting as the critical link that governs the continuous exchange of moisture and latent heat between the Earth's surface and the atmosphere (Trenberth et al., 2003a). While the latent heat released during condensation is a fundamental driver of global atmospheric circulation (Allan et al., 2020), precipitation itself constitutes the vital water input for terrestrial systems. As the principal source of soil moisture and groundwater, it fundamentally dictates the land-surface water budget, thereby regulating ecosystem functions and sustainable water availability (Oki and Kanae, 2006). The dynamic nature of the hydrological cycle is further underscored by precipitation extremes; excessive rainfall triggers devastating floods, while prolonged deficits lead to droughts. These deficits deplete soil moisture and shift surface energy partitioning, often culminating in complex drought–heatwave compound extremes (Miralles et al., 2019; Zscheischler et al., 2020).

The variability of precipitation spans a wide spectrum of time scales, from interannual to sub-daily, with distinct physical processes governing the hydrological cycle at each scale. Variations at interannual, seasonal, intraseasonal, and synoptic scales are associated with ENSO (He and Li, 2019; Huang and Xie, 2015) , monsoons (Wang et al., 2012; Wang and Ding, 2008), the Madden–Julian Oscillation (Jiang et al., 2020; Zhang, 2005), and extratropical cyclones (Catto et al., 2012; Hawcroft et al., 2012; Pfahl and Wernli, 2012a), respectively. Beyond these large-scale oscillations, sub-daily variability constitutes a significant fraction of the total precipitation budget. Satellite retrievals indicate that sub-daily internal variability explains more than 50% of the total internal variability during the boreal summer (Ahn et al., 2022). The diurnal cycle, as the dominant component of this sub-daily variance, represents one of the most fundamental modes of the climate system, governed by the 24-hour periodicity of Earth's rotation (Christopoulos and Schneider, 2021; Dai, 2001; Yang and Slingo, 2001).

Over land, the diurnal cycle of precipitation often peaks in the afternoon and is intrinsically linked to the surface energy balance. As incoming solar radiation maximizes around noon, the surface responds through intensified sensible and latent heat fluxes. The sensible heat flux deepens the planetary boundary layer (PBL), while the latent heat flux supplies the necessary moisture to the lower atmosphere (Dai, 2024). Specifically, turbulent mixing within the PBL enhances the equivalent potential temperature of the lower atmosphere, facilitating the accumulation of convective available potential energy (CAPE). Concurrently, the weakening of the low-level inversion and the upward moisture transport reduce convective inhibition (CIN), ultimately triggering convection (Dai, 2024; Dai et al., 1999). However, a characteristic lag of 3–6 hours exists between peak surface fluxes and the precipitation maximum. This delay is attributed to the initial development of shallow cumulus, which experience lateral and cloud-top entrainment of dry environmental air into the convective plumes. This process dilutes the buoyancy within the core of the rising air and suppresses its vertical growth (Stirling and Stratton, 2012; Tian and Kuang, 2016). Consequently, a transitional period is required for shallow convection to moisten the lower free atmosphere and further erode CIN. Through these complex land-atmosphere interactions, the precipitation maximum over most terrestrial regions is realized in the late afternoon to early evening (15–21 LST; Dai et al. 1999; Watters et al. 2021).

https://doi.org/10.5194/egusphere-2026-2867
Preprint. Discussion started: 3 June 2026

However, this surface-heating-driven mechanism is not universally dominant. In regions where large-scale dynamical forcing governs precipitation, diurnal characteristics diverge significantly from the solar-driven pattern. For instance, over the U.S. Great Plains (GP), the nocturnal low-level jet (LLJ) intensifies after sunset due to boundary layer decoupling and transports moist air northward from the Gulf of Mexico. The resulting convergence at the poleward terminus of the jet triggers elevated convection and the propagation of mesoscale convective systems (MCSs), leading to a precipitation peak between midnight and early morning (Higgins et al., 1997; Shapiro et al., 2016). Over the Maritime Continent, daytime convection initiated over land propagates offshore via land breezes and gravity waves, resulting in nocturnal-to-early morning rainfall over coastal waters (Love et al., 2011; Lu et al., 2021; Mori et al., 2004). Furthermore, diurnal cycles vary by precipitation type; large-scale precipitation (LSP) generally exhibits a weak diurnal amplitude with a dawn peak (approximately 06 LST), whereas convective precipitation (CP) displays a robust diurnal cycle peaking in the late afternoon (16–20 LST). Since total precipitation (TP) is the aggregate of these components, the timing of the TP peak often precedes that of CP by 1–2 hours, reflecting the complex interplay between different precipitation regimes (Dai, 2001; Dai and Trenberth, 2004).

In contrast to terrestrial regions, the oceanic diurnal precipitation maximum typically occurs in the early morning (04–08 LST), with a diurnal amplitude generally weaker than that over land (Dai, 2001; Dai et al., 2007). Over coastal waters, strong daytime heating over adjacent landmasses drives a land–sea breeze circulation that induces low-level convergence over the ocean during the night, resulting in an early-morning precipitation peak (Deser and Smith, 1998a). In the tropical and open oceans where continental influence is minimal, differential longwave radiative cooling between cloudy and clear regions during the night enhances nocturnal destabilization and low-level convergence (Gray and Jacobson, 1977). Furthermore, spatial phase differences in semidiurnal pressure tides can further intensify this early-morning convergence, playing a crucial role in the diurnal timing of oceanic precipitation (Dai et al., 1999).

Given that the diurnal cycle of precipitation results from the complex coupling of radiation, convection, and boundary layer processes, it serves as a critical benchmark for evaluating the physical fidelity of climate models (Cui et al., 2021; Watters et al., 2021). While climate models can reasonably reproduce precipitation characteristics at seasonal and interannual scales, they consistently struggle to simulate a realistic diurnal cycle (Christopoulos and Schneider, 2021; Dong et al., 2023). For instance, CMIP5 and CMIP6 models typically produce a diurnal peak 3–5 hours earlier than observations over land, accompanied by a substantial inter-model spread in amplitude. Over the ocean, although the simulated phase is more comparable to observations, the amplitude remains significantly underestimated, a persistent bias across multiple CMIP generations (Christopoulos and Schneider, 2021; Tang et al., 2021). Many models employ CAPE-based convective triggers that activate convection prematurely in response to boundary layer heating. Furthermore, because these schemes often diagnose shallow and deep convection independently, they fail to represent the gradual transition between these two stages (Freitas et al., 2021; Yang et al., 2021). This leads to the well-known "too frequent, too light" problem in diurnal precipitation and an underestimation of the diurnal cycle amplitude (Dai, 2006a; Stephens et al., 2010). Additionally, coarse spatial resolution hinders the proper representation of MCS initiation and propagation, particularly in regions dominated by nocturnal peaks

https://doi.org/10.5194/egusphere-2026-2867
Preprint. Discussion started: 3 June 2026

(Song et al., 2024). Reanalysis datasets inherit these systemic problems, as precipitation fields largely rely on model physics with limited sub-daily data assimilation, leading to the same premature peaks found in climate models (Dai and Trenberth, 2004; Watters et al., 2021).

Satellite remote sensing has been widely utilized to address the limitations inherent in climate models and reanalyses. In particular, the Tropical Rainfall Measuring Mission (TRMM) launched in 1997, followed by the Global Precipitation Measurement (GPM) mission, has provided unprecedented global observations of the vertical structure and spatiotemporal variability of precipitation (Kummerow et al., 1998; Zhao et al., 2014a). These high-resolution datasets serve as an essential benchmark for validating model physics and reanalysis performance. With the proliferation of diverse satellite products (e.g., GPM-based IMERG, microwave-morphing-based CMORPH, and GSMaP), numerous intercomparisons of the diurnal precipitation cycle have been conducted (Afonso et al., 2020; Janowiak et al., 2005). However, differences in retrieval algorithms and temporal sampling strategies among these products lead to significant discrepancies in their captured diurnal characteristics (Pradhan et al., 2025; Watters et al., 2021). Furthermore, because satellite-based precipitation estimations rely on indirect proxies (e.g., upper-level ice scattering and cloud-top temperatures) rather than direct surface measurements, they frequently exhibit a systematic phase delay in the diurnal peak relative to ground-based observations (Guilloteau et al., 2018; Petković et al., 2018; Sun et al., 2018).

As discussed above, both satellite and reanalysis datasets possess inherent biases in their representation of the diurnal precipitation cycle. Although various ground-based studies have attempted to diagnose these issues, several critical gaps remain. First, global-scale diurnal cycle analyses have relied on synoptic present weather codes (WMO ww codes from SYNOP reports) rather than direct precipitation measurements (Dai, 2001; Dai et al., 2007). Moreover, studies using hourly precipitation observations are limited to specific regions or a small number of observation sites (Dai, 2024; Tang et al., 2021), leaving a gap in globally representative, ground-observation-based benchmarks. Second, intercomparisons of satellite products have been confined to comparisons among satellite datasets (Pradhan et al., 2025), and no study simultaneously evaluated the diurnal cycle performance of multiple satellite products against a ground-based observation reference. Third, while phase shifts in individual reanalyses such as ERA5 and MERRA-2 have been reported (Dai, 2024; Watters et al., 2021), a comprehensive evaluation remains lacking. Given that convective parameterization has been identified as a primary determinant of diurnal cycle fidelity in global models (Dirmeyer et al., 2012), systematic differences among reanalysis products with distinct convective schemes remains insufficiently explored. This is particularly relevant for the recently improved JRA-3Q, which features an updated convective parameterization (Kosaka et al., 2024). In particular, the systematic diagnosis of phase shifts through the partitioning of convective and large-scale precipitation remains unexplored across these diverse datasets.

To advance the understanding of the precipitation diurnal cycle and rigorously evaluate the performance of current satellite and reanalysis datasets, this study utilizes hourly observations from 6,824 ground-based stations over the Northern Hemisphere (NH) land regions. We evaluate sub-daily precipitation characteristics across five satellite products (IMERG, TRMM 3B42, CMORPH, GSMaP, and MSWEP) and four reanalysis datasets (ERA5, JRA-3Q, MERRA-2, and NARR). Unlike previous

https://doi.org/10.5194/egusphere-2026-2867
Preprint. Discussion started: 3 June 2026

studies that focused primarily on the phase and amplitude of the diurnal cycle, this work first quantifies the fraction of TP variability explained by sub-daily fluctuations. We then diagnose the relative contributions of the diurnal (24-hour), semi-diurnal (12-hour), and higher-order harmonics within the sub-daily band to evaluate the harmonic balance inherent in each product. Furthermore, the study compares the dominant diurnal phase and amplitude across all datasets and investigates the physical drivers of phase shifts, particularly in reanalysis products. Finally, radiosonde observations from the Atmospheric Radiation Measurement (ARM) Southern Great Plains (SGP) site are integrated to explore the boundary layer and convective processes underlying the systematic biases identified in the reanalyses.

The remainder of this paper is organized as follows. Section 2 describes the ground-based observations, satellite products, and reanalysis datasets utilized in this study. Section 3 describes the analytical methods, including sub-daily variance decomposition and harmonic analysis. Section 4 presents the key results, including the decomposition of global precipitation variability across various time scales, an intercomparison of diurnal cycle phase and amplitude, and an analysis of diurnal characteristics by precipitation type. This section also includes a comprehensive case study at the ARM SGP site and two additional representative locations namely a site in the southeastern United States and NH regional mean, to diagnose the underlying physical mechanisms. Finally, Section 5 summarizes the major findings and discusses their broader implications for climate modelling and future observations.

2 Data

2.1 Ground-based observations

2.1.1 Global precipitation observations

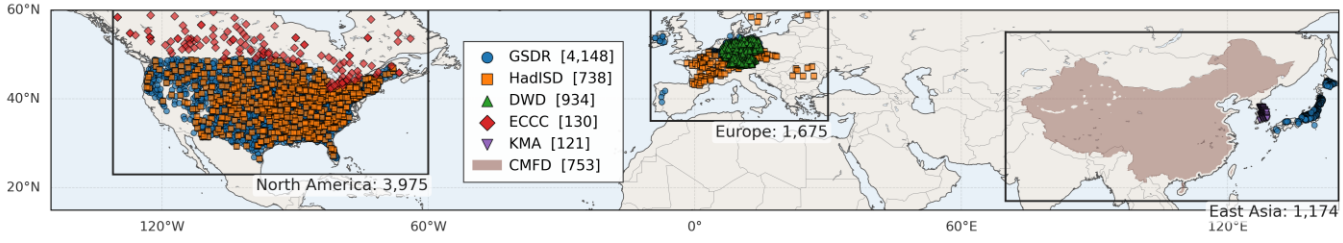

Figure 1: Locations of ground-based precipitation observations over the Northern Hemisphere. Symbols denote point-based observation stations from each dataset, and the shaded area indicates the spatial coverage of the gridded CMFD dataset, which is a fusion product combining station observations with reanalysis data. Bracketed numbers indicate the total number of stations or the number of stations to construct the gridded CMFD product. Boxes delineate the three major regions of station concentration (North America, Europe, and East Asia), with the total number of observations within each region indicated below each box label.

Ground-based rain gauge observations provide direct surface measurements that are widely used as the reference for evaluating satellite and reanalysis datasets (e.g., Dai et al., 2007; Tang et al., 2021; Xie et al., 2007). The observational network comprises six distinct data sources (Table 1): (1) a subset of the Global Sub-Daily Rainfall Dataset (GSDR; Lewis et al., 2019),

https://doi.org/10.5194/egusphere-2026-2867
Preprint. Discussion started: 3 June 2026

which provides quality-controlled hourly precipitation from approximately 23,000 gauge stations worldwide, (2) the Hadley Centre Integrated Surface Database (HadISD; Dunn et al., 2016), containing sub-daily precipitation observations from synoptic weather stations with comprehensive quality control, hourly precipitation datasets from (3) Germany Deutscher Wetterdienst (DWD), (4) Environment and Climate Change Canada (ECCC), and (5) Korea Meteorological Administration (KMA) national weather stations, and (6) China Meteorological Forcing Dataset version 1.6 (CMFD; He et al., 2020), which provides gridded 3-hourly precipitation at 0.1° resolution over China based on a fusion of 753 China Meteorological Administration (CMA) station observations with satellite based data. These precipitation observations have 1- or 3-hourly temporal resolution.

The spatial distribution of gauge observations exhibits substantial regional heterogeneity, with station density predominantly concentrated in the NH, particularly over North America, Europe, and East Asia. To ensure sufficient temporal representativeness, only stations with complete 3-hourly records for at least 3 boreal summers (JJA; 92 days × 3 years = 276 days) are retained. The resulting station network is concentrated in NH mid-latitude land regions, reflecting the global heterogeneity of long-term sub-daily gauge availability. We therefore restrict quantitative validation against ground observations to NH land, while presenting global maps in subsequent figures to characterize the spatial structure of inter-product differences. Over ocean and SH land, where direct validation is not feasible, multi-satellite (MS) and multi-model (MM) means serve as references for relative inter-product comparison rather than absolute accuracy assessment.

To minimize the influence of coastal precipitation regimes, which are governed by land–sea breeze circulations and offshore propagation of convective systems that are not representative of continental diurnal forcing, stations located within 50 km of the coastline are excluded based on their coordinates. The same distance criterion is applied to CMFD grid cells using their centre coordinates. After applying both the coastal exclusion and the minimum record length criteria described above, the final dataset comprises 6,071 point-based stations (North America: 3,975, Europe: 1,675, East Asia: 421) and 753 CMFD station-based gridded observations over China, yielding a combined total of 6,824 observation records (Fig.1). To minimize inconsistencies in spatial representativeness across datasets, the station statistics are spatially averaged onto a 0.5° × 0.625° grid, and CMFD grid cells are remapped to the same grid, corresponding to the coarsest spatial resolution among the gridded products (MERRA-2). This procedure is consistent with the spatial harmonization described in Section 3.

https://doi.org/10.5194/egusphere-2026-2867
Preprint. Discussion started: 3 June 2026

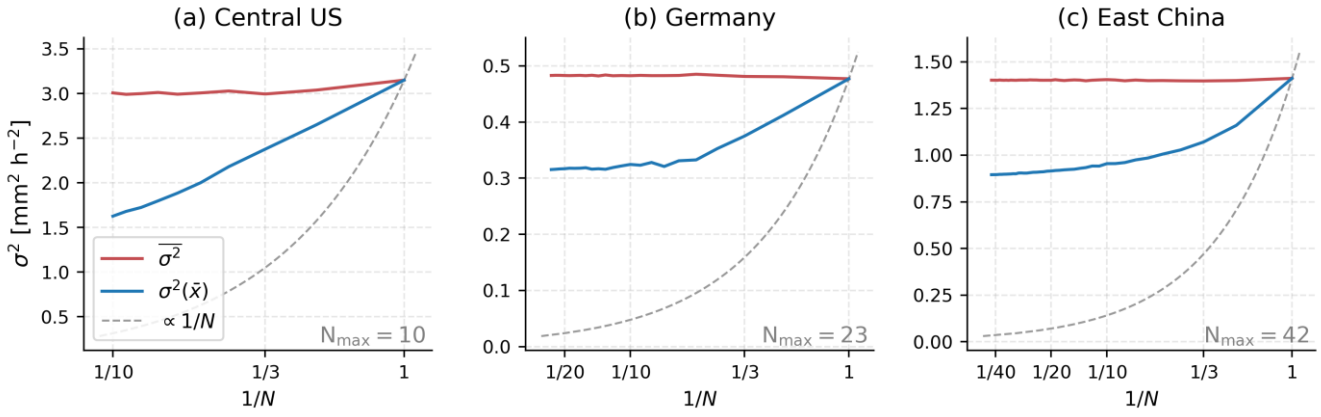

Figure 2: Sensitivity of the grid-cell averaged sub-daily precipitation variance (σ^2) to the number of stations (N), evaluated at single representative 0.5° × 0.625° grid cells in (a) Central US (33.0°N, 96.9°W), (b) Germany (51.0°N, 10.0°E), and (c) East China (31.5°N, 110.8°E). For each N from 1 to N_{max}, all possible combinations of station subset are used to compute σ^2 under two approaches: $\overline{\sigma^2}$, in which variance is computed at each station individually and subsequently averaged across the selected stations (red line); and $\sigma^2(\bar{x})$, in which station time series are first spatially averaged and variance is subsequently computed from the resulting mean time series (blue line). The dashed line indicates the theoretical 1/N scaling expected when variance decreases solely as a result of averaging independent samples.

Sub-daily precipitation variance is computed independently at each ground-based station prior to aggregation within each grid cell (hereafter, variance-then-averaging approach). An alternative approach, in which station time series are first averaged at each time step across all contributing stations within a grid cell before variance is computed from the resulting composite time series (hereafter, averaging-then-variance approach), would introduce a systematic dependence on the number of contributing stations (N): the variance of the mean of N random variables is proportional to 1/N of the individual variance. Consequently, grid-cell variance estimates derived from the averaging-then-variance approach would be biased as a function of station density. The attenuation of temporal variability through time-step-wise averaging of station time series within a given area has been documented in prior studies (Osborn and Hulme, 1997), and spatial smoothing of precipitation fields is known to reduce high-frequency variance (Light et al., 2022). The averaging-then-variance approach is therefore inappropriate for diagnosing sub-daily variability across regions with heterogeneous station densities.

The variance-then-averaging approach adopted here follows the "statistic-then-grid" order of operations employed in widely used observational datasets such as HadEX2 and GHCNDEX (Donat et al., 2013), and is consistent with the approach advocated for model evaluation studies involving spatial remapping (Gibson et al., 2019). Figure 2 illustrates the sensitivity of grid-cell-averaged sub-daily precipitation variance to N over three representative grid cells (Central US, Germany, and East China), where station subsets of increasing size N are randomly drawn from the full set of N_{max} available stations within each region. For each subset, variance is estimated using both approaches: the variance-then-averaging estimate ($\overline{\sigma^2}$), in which variance is computed independently at each station and subsequently averaged, and the averaging-then-variance estimate ($\sigma^2(\bar{x})$), in which station time series are first averaged at each time step before variance is computed from the resulting

https://doi.org/10.5194/egusphere-2026-2867
Preprint. Discussion started: 3 June 2026

composite time series. The variance-then-averaging estimate ($\overline{\sigma^2}$) remains approximately constant across all values of N, whereas the averaging-then-variance estimate ($\sigma^2(\bar{x})$) decreases monotonically as N increases. The rate of decrease in the latter is more gradual than the theoretical $1/N$ scaling expected under the assumption of spatially independent observations, reflecting the positive spatial correlations among neighbouring stations that partially offset the dilution effect. These results confirm that the averaging-then-variance approach systematically underestimates sub-daily variability as a function of station density, and support the validity of the variance-then-averaging approach adopted in this study.

	Time resolution	Spatial resolution	Time period	Reference
GSDR	1 h	Point sites (4,148)	1950–present	Lewis et al. 2019
HadISD	1/3 h	Point sites (738)	1973–present	Dunn et al. 2016
DWD stations	1 h	Point sites (934)	1951–present	DWD
ECCC stations	1 h	Point sites (130)	1961–present	ECCC
KMA stations	1 h	Point sites (121)	1980–present	KMA
CMFD	3 h	0.1° × 0.1° (93,133 grid cells)	1979–present	He et al. 2020

Table 1: Description of ground-based precipitation datasets. The numbers in parentheses in the spatial resolution column indicate the total number of stations used in this study.

2.1.2 SGP site observations

Observational data from the Atmospheric Radiation Measurement (ARM) Southern Great Plains (SGP) observatory, located near Lamont, Oklahoma (36.6°N, 97.5°W, 306 m elevation), are used to investigate the physical processes underlying the diurnal cycle of precipitation. The ARM SGP site provides qualified long-term observations of precipitation, atmospheric state variables, and surface energy fluxes that are essential for understanding the mechanisms of diurnal precipitation variability over the central United States.

Hourly precipitation is obtained from the ARM Best Estimate Atmospheric Measurements (ARMBEATM) product (Xie et al. 2010). ARMBEATM provides the best estimate of atmospheric states specifically tailored for evaluating global climate models. The precipitation measurements are obtained from both standard and optical rain gauges at the central facility. High-frequency raw measurements at 30-second or 1-minute frequency are temporally averaged to an hourly resolution to ensure consistency with model output. These single-point measurements provide quality-controlled precipitation records suitable for a detailed analysis of the diurnal cycle, although they may not fully capture the spatial variability within grided model domains.

The ARM Variational Analysis (VARANAL) product (Tang et al., 2019; Xie et al., 2007; Zhang et al., 2001) provides large-scale forcing fields derived from ground-based observations constrained by ARM surface and top-of-atmosphere measurements. VARANAL was originally designed to drive single-column models, cloud-resolving models, and large-eddy simulations by providing atmospheric boundary conditions derived from consistent estimates of atmospheric state variables and surface fluxes. The SGP continuous forcing dataset combines two data streams, sgp60varanarapC1.c1 (based on Rapid

https://doi.org/10.5194/egusphere-2026-2867
Preprint. Discussion started: 3 June 2026

Refresh model) and sgp60varanarucC1.c1 (based on Rapid Update Cycle model), representing conditions averaged over a domain of approximately 370 km × 300 km centered on the SGP central facility at 1-hourly temporal resolution. In this study, surface sensible heat flux and latent heat flux from VARANAL are utilized to examine their relationship with the diurnal precipitation cycle.

Upper-air atmospheric conditions are characterized using radiosonde observations from the Integrated Global Radiosonde Archive (IGRA) version 2 (Durre et al., 2006, 2016) for station USM00074646 located at Lamont, Oklahoma (36.6°N, 97.5°W, 306 m elevation), which provides 6-hourly soundings from 2000 to present. The IGRA2 data is used in the place of upper-air measurements from ARMBEATM to calculate CAPE, CIN, moist static energy (MSE), and atmospheric precipitable water tendency (dPW). All observed variables at SGP site are utilized for the period 2000–2023, using available days within this period. Surface sensible and latent heat fluxes from VARANAL are used as 3-hourly averages, while precipitation data is used as 3-hourly accumulations.

2.2 Satellite-based datasets

The Integrated Multi-satellite Retrievals for GPM (IMERG) Version 07B Final Run (Huffman et al., 2023) is a unified algorithm that intercalibrates, merges, and interpolates precipitation estimates from multiple sources including passive microwave (PMW) retrievals from the GPM constellation satellites, microwave-calibrated infrared (IR) satellite estimates, and monthly gauge analyses. IMERG provides global precipitation estimates at 0.1° spatial resolution and 30-minute temporal resolution from 2000 to present, using the GPM Core Observatory and Tropical Rainfall Measuring Mission (TRMM) satellites as calibration references. The algorithm employs Lagrangian interpolation with motion vectors derived from geostationary IR imagery to propagate PMW-observed precipitation fields forward and backward in time, then applies a Kalman filter (Joyce and Xie, 2011) to combine these fields with IR estimates into weighted precipitation estimates. The Final Run incorporates monthly gauge adjustments from the Global Precipitation Climatology Centre (GPCC) Version 3 (Adler et al., 2018; Huffman et al., 2023), applying spatially varying ratio multipliers that remain constant throughout each month to correct the bias in satellite-based estimates.

The Tropical Rainfall Measuring Mission (TRMM) Multi-satellite Precipitation Analysis (TMPA) version 7 real-time product (3B42RT) provides near-real-time precipitation estimates at 0.25° × 0.25° spatial resolution and 3-hourly temporal resolution between 50°N and 50°S (Huffman et al., 2007). TRMM 3B42RT combines PMW precipitation estimates from multiple low-Earth-orbit satellites—including the TRMM Microwave Imager (TMI), Advanced Microwave Scanning Radiometer (AMSR) on AQUA, Special Sensor Microwave Imager (SSM/I) on Defense Meteorological Satellite Program (DMSP) satellites, and Advanced Microwave Sounding Unit (AMSU) on NOAA satellites—with IR observations from geostationary satellites including the Geostationary Operational Environmental Satellites (GOES), Meteosat, and Geostationary Meteorological Satellite (GMS). The real-time product has approximately 7-hour latency and does not include gauge adjustments, making it less accurate than the research-grade product (3B42) but suitable for operational applications

https://doi.org/10.5194/egusphere-2026-2867
Preprint. Discussion started: 3 June 2026

(Chen et al. 2013). Version 7, released in 2013, incorporated Special Sensor Microwave Imager/Sounder (SSMIS) data and improved PMW retrieval algorithm (GPROF 2010; Kummerow et al., 2015) and IR brightness temperature calibration compared to version 6 (Yong et al., 2014).

The CPC (Climate Prediction Center) Morphing Technique (CMORPH; Joyce et al., 2004) produces global precipitation estimates by integrating PMW precipitation retrievals from multiple low earth orbit (LEO) satellites (TMI on TRMM, AMSR on AQUA, SSM/I and SSMIS on DMSP F-13–F-18, AMSU and MHS on NOAA-15–19 and MetOp-A/B, and MWRI on FY-3B). Unlike other satellite products that directly combine PMW and IR estimates, CMORPH uses cloud motion vectors derived from consecutive geostationary (GEO) IR brightness temperature images to realize the propagation of PMW retrievals through time and space. The morphing technique employs a time-weighting scheme that blends forward- and backward-propagated PMW estimates, with weights inversely proportional to the temporal distance from the observation time. This approach yields precipitation estimates at 30- minute intervals, effectively bridging the gaps between infrequent PMW overpasses.

This study uses the bias-corrected CMORPH Climate Data Record (CDR) Version 1.0 (Xie et al., 2017), which applies systematic bias correction to the raw satellite estimates. Over land, bias correction is performed through daily-based probability density function (PDF) matching against the CPC Unified Daily Gauge Analysis, which adjusts the statistical distribution of satellite-estimated precipitation rates to match ground-based observations. Over ocean, the Global Precipitation Climatology Project (GPCP) pentad (5-day) is used to carry out the PDF matching technique with following two steps: first using climatological correction based on a 15-year dataset, then applying real-time refinement using a 31-day moving window (Xie et al. 2017). The adjustment coefficients, calculated as the ratio between the mean reference field (CPC gauge or GPCP pentad) and the mean raw CMORPH, are downscaled from daily 0.25° resolution to the native 30-min 8 km resolution. The dataset has a global coverage from 60°S to 60°N spanning from January 1998 to the present.

The Global Satellite Mapping of Precipitation (GSMaP) version 8 gauge-calibrated product (GSMaP_Gauge) provides global hourly precipitation estimates at 0.1° × 0.1° spatial resolution between 60°N and 60°S (Kubota et al., 2020). GSMaP retrieves precipitation using PMW radiometer data from the GPM constellation and integrates them with IR observations from geostationary satellites via a Kalman filtering algorithm, which propagates PMW estimates both forward and backward in time (Ushio et al., 2009). The gauge-calibrated version further refines these satellite-based estimates by incorporating daily rain gauge data from the NOAA CPC Unified Daily Gauge Analysis to enhance accuracy over land (Kubota et al., 2022; Lu and Yong, 2020; Mega and Ushio, 2017). Version 8, released in December 2021, introduces substantial improvements including updated PMW retrieval databases, enhanced orographic rainfall estimation, and a normalization module to homogenize retrievals among multiple microwave sensors (Gao et al., 2024; Tashima et al., 2021; Yamamoto and Kubota, 2022). Additionally, the retrieval domain has been extended toward the poles during PMW overpasses, thereby improving precipitation estimates in high-latitude regions.

https://doi.org/10.5194/egusphere-2026-2867
Preprint. Discussion started: 3 June 2026

The Multi-Source Weighted-Ensemble Precipitation (MSWEP) Version 2.8 (Beck et al., 2019) is a merged dataset that integrates gauge observations, satellite products, and reanalysis outputs using a weighted-ensemble methodology. The dataset combines three non-gauge products (ERA5, IMERG, and GridSat) at 3-hour time step and 0.1° spatial resolution. Weights are assigned based on station density for gauge-based components and comparative skill against nearby gauges for satellite and reanalysis components. All possible combinations of datasets are merged through weighted averaging, with cumulative weights calculated to represent the total information content. To mitigate spurious light rainfall and the underestimation of heavy precipitation, Cumulative distribution function (CDF) matching is applied.

MSWEP incorporates systematic daily gauge corrections utilizing multiple sources including GHCN-D and GSOD through a multiplicative approach that preserves sub-daily distributions. Notably, the dataset accounts for regional variations in gauge reporting times (ranging globally from 00Z to 12Z), thereby minimizing temporal mismatches between gridded estimates and gauge observations. Monthly corrections are applied using the CHELSA (Karger et al., 2017), replacing the WorldClim-based corrections used in earlier versions. A unique attribute of MSWEP is its correction for systematic terrestrial biases (e.g., gauge undercatch and orographic effects), which is achieved by inferring catchment-average precipitation from observed river discharge at 13,762 catchments globally. The dataset provides global coverage at 0.1° and 3-hourly resolution from 1979 onward.

Name	Time resolution	Spatial resolution	Time period	PMW sensors	IR sensors	Correction	Reference
IMERG V7	0.5 h	0.1° × 0.1°	2000–present	GMI, TMI, AMSR-E, AMSR2, SSMI, SSMIS, AMSU, MHS, ATMS	GMS/MTSat/Himawari, GOES-E, GOES-W, Meteosat	GPCC (M)	Huffman et al. 2023
TRMM 3B42RT V7	3 h	0.25° × 0.25°	2000–2019	TMI, AMSR, SSM/I, SSMIS, AMSU, MHS	GOES, Meteosat, GMS	None	Huffman et al. 2007
CMORPH-CDR	1 h	0.25° × 0.25°	1998–present	TMI, AMSR, SSM/I, SSMIS, AMSU, MHS, MWRI	GOES, Meteosat, GMS	CPC (D), GPCP (5D, ocean)	Xie et al. 2017
GSMaP V8	1 h	0.1° × 0.1°	1998–present	GMI, TMI, AMSR-E, AMSR2, SSM/I, SSMIS, MADRAS, AMSU-A/B, MHS, ATMS	MTSAT/GMS, GOES, Meteosat	CPC (D)	Kubota et al. 2020
MSWEP V2.8	3 h	0.1° × 0.1°	1979–present	Satellite (IMERG, GridSat), Reanalysis (ERA-5), Gauge		GHCN-D (D), GSOD (D), CHELSA (M),	Beck et al. 2019

https://doi.org/10.5194/egusphere-2026-2867
Preprint. Discussion started: 3 June 2026

Table 2: Description of satellite-based precipitation datasets. Primary data sources include passive microwave (PMW) and infrared (IR) sensors. Temporal resolution of bias correction is indicated in parentheses (D: daily; 5D: 5-day pentad; M: monthly).

2.3 Reanalysis datasets

The European Centre for Medium-Range Weather Forecasts (ECMWF) Reanalysis Version 5 (ERA5; Hersbach et al., 2020) provides global hourly atmospheric estimates from 1950 to present. It employs the Integrated Forecasting System (IFS) Cycle 41r2 with a hybrid incremental four-dimensional variational (4D-Var) data assimilation scheme, assimilating observations with 12-hour assimilation windows (09–21 UTC and 21–09 UTC). The atmospheric model has 0.25° × 0.25° horizontal resolution with 137 hybrid sigma-pressure vertical levels extending from the surface to 0.01 hPa. ERA5 reanalysis incorporates the Hydrology Tiled ECMWF Scheme for Surface Exchanges over Land (H-TESSEL) to simulate land surface variables, utilizing a weakly coupled land data assimilation system to adjust soil moisture and snow depth with screen-level temperature and humidity observations (Balsamo et al., 2009). Notably, ERA5 precipitation is derived from 18-hour forecasts initialized twice daily (06 and 18 UTC), with hourly outputs accumulated from the first 12 hours (1–12 hour lead time) (Lavers et al., 2022; Soci et al., 2024). Each hourly value corresponds to a forecast lead time of 1–12 hours, depending on its temporal proximity to the initialization. Crucially, precipitation observations are not directly assimilated; instead, precipitation is generated as a diagnostic output from the model physics.

The Modern-Era Retrospective Analysis for Research and Applications, Version 2 (MERRA-2), is NASA's global atmospheric reanalysis produced by the Global Modeling and Assimilation Office (GMAO), providing data from 1980 to the present at 0.5° × 0.625° horizontal resolution with hourly temporal resolution (Gelaro et al., 2017). The system utilizes the Goddard Earth Observing System Model, Version 5 (GEOS-5; Molod et al., 2015) with a 6-hourly assimilation window based on the Gridpoint Statistical Interpolation (GSI) scheme (Wu et al., 2002) and Incremental Analysis Update (IAU) methodology (Bloom et al., 1996). The assimilation system incorporates extensive conventional and satellite-based atmospheric observations, including modern microwave sounders such as the Advanced Microwave Sounding Unit (AMSU-A), Advanced Technology Microwave Sounder (ATMS), and Microwave Humidity Sounder (MHS) that provide atmospheric temperature and humidity profiles, and hyperspectral infrared radiance instruments such as the Atmospheric Infrared Sounder (AIRS), Infrared Atmospheric Sounding Interferometer (IASI), and Cross-track Infrared Sounder (CrIS) that provide temperature and moisture sounding information. Precipitation fields are generated as a diagnostic output from model physics, without direct correction or assimilation of precipitation observations.

The Japanese Reanalysis for Three Quarters of a Century (JRA-3Q) is the third global atmospheric reanalysis produced by the Japan Meteorological Agency (JMA), covering September 1947 to present at TL479 (~0.375°) horizontal resolution (Kosaka et al., 2024). JRA-3Q builds upon its predecessor JRA-55 (Kobayashi et al., 2015), by incorporating three major updates: (1) an updated forecast model and data assimilation system based on the JMA operational numerical weather prediction system since December 2018, (2) improved boundary conditions, including updated sea surface temperature and sea ice datasets, and (3) the assimilation of additional observations including Global Navigation Satellite System (GNSS)

https://doi.org/10.5194/egusphere-2026-2867
Preprint. Discussion started: 3 June 2026

zenith total delay (ZTD) for atmospheric water vapor, GNSS radio occultation (up to 60 km altitude), airport surface pressures, and hyperspectral infrared sounder radiances (e.g., AIRS, IASI, CrIS) for temperature and humidity profiles. The reanalysis employs a 4D-Var data assimilation system using the JMA Global Spectral Model (GSM), with assimilation cycles every 6 hours (00, 06, 12, and 18 UTC).

The North American Regional Reanalysis (NARR), produced by NOAA's National Centers for Environmental Prediction (NCEP), provides regional atmospheric data over North America from 1979 to present at ~32 km horizontal resolution and 3-hourly temporal resolution (Mesinger et al., 2006). NARR employs the NCEP Eta Model with a three-dimensional variational (3D-Var) data assimilation system, cycling every 3 hours where the 3-hour forecast from the previous cycle serves as the first guess. Unlike global reanalyses, NARR assimilates precipitation observations via a latent heating nudging technique (Lin et al., 1999). This method converts observed precipitation into vertical profiles of latent heating, which are then nudged into the model's temperature tendency equation during the forecast step. Over the continental United States, the system assimilates the Hourly Precipitation Dataset (HPD) and Parameter-elevation Regressions on Independent Slopes Model (PRISM; Daly et al., 1994) daily precipitation incorporating diurnal patterns from the Global Reanalysis 2 (GR2) forecasts when the HPD data is unavailable. For Canada and Mexico, GR2-based diurnal patterns are similarly applied to daily national gauge data. Over oceanic regions (south of 27.5°N), Climate Prediction Center Merged Analysis of Precipitation (CMAP) pentad data (Xie and Arkin, 1997) are assimilated; however, north of 42.5°N, precipitation assimilation is omitted due to uncertainties in the CMAP product in high latitudes.

Name	Time resolution	Spatial resolution	Time period	DA cycle	Precipitation DA	Moisture DA	Reference
ERA5	1 h	0.25° × 0.25°	1950–present	12 h (4D-Var)	None (forecast derived)	Satellite radiance (AMSU-A, MHS, IASI, CrIS), GPSRO	Hersbach et al., 2020
MERRA-2	3 h	0.5° × 0.625°	1980–present	6 h (3D-Var)	None (forecast derived)	Satellite radiance (AMSU-A, ATMS, MHS, AIRS, IASI, CrIS), GPSRO	Gelaro et al., 2017
JRA-3Q	3 h	0.375° × 0.375°	1947–present	6 h (4D-Var)	None (forecast derived)	Satellite radiance (AIRS, IASI, CrIS), GNSS ZTD	Kosaka et al., 2024
NARR	3 h	0.3° × 0.3°	1979–present	3h (3D-Var)	1h (latent heating nudging): Gauge (HPD, 1979-2002), Radar+gauge (2003-present, US), CMAP pentad (ocean)	Satellite radiance, conventional observation	Mesinger et al., 2006

Table 3: Description of reanalysis precipitation datasets.

https://doi.org/10.5194/egusphere-2026-2867
Preprint. Discussion started: 3 June 2026

3 Methods

To ensure consistent intercomparison across all precipitation datasets, we perform both spatial and temporal harmonization. All datasets, regardless of their original format (gridded products, point observations, or reanalysis outputs), are remapped to a common spatial resolution of 0.5° × 0.625° (matching the MERRA-2 grid) using bilinear interpolation. This method efficiently transforms heterogeneous inputs onto a unified grid while preserving spatial continuity, thereby minimizing scale-dependent representativeness errors (Gervais et al., 2014; Tustison et al., 2001).

All precipitation products are standardized to 3-hourly accumulated totals (mm (3 h)$^{-1}$). Datasets provided as precipitation rates (e.g., mm s^{-1}, kg m^{-2} s^{-1}) are converted to mm h^{-1} and accumulated over 3-hour windows, while those originally supplied as 3-hourly accumulations are used directly. This harmonization protocol ensures that discrepancies between products reflect intrinsic variations in retrieval algorithms and data sources rather than inconsistencies in resolution or units (Pradhan et al., 2025). After this data pre-processing, diurnal cycle analyses are restricted to rainy days (daily precipitation ≥ 0.275 mm day^{-1}) to exclude unreliable signals from weak precipitation signals (Watters et al., 2021).

This study focuses exclusively on the boreal summer season (June–August; JJA), when diurnal precipitation variability is strongest over Northern Hemisphere land. Analysis periods vary due to data availability: CMORPH and GSMaP (1998–2022), TRMM 3B42RT (2000–2019), IMERG and MSWEP (2000–2023), and all reanalysis products (2000–2023). Previous studies suggest that a stable diurnal cycle can be derived from just a few years of data (Covey et al., 2016; Dai et al., 2009; Tang et al., 2021), supporting the robustness of cross-period comparisons despite differences in temporal coverage among datasets. To further assess the sensitivity of the results to the choice of analysis period, we conducted sensitivity tests by restricting selected datasets to non-overlapping sub-periods (e.g., CMORPH: 1998–2007 and 2013–2022) and comparing the resulting diurnal phase estimates against those derived from the full analysis period. The mean phase difference between sub-periods and the full-period analysis is less than 1 hour across all tested datasets, confirming that the diurnal cycle characteristics are not substantially sensitive to the choice of analysis period (not shown). We therefore utilize the maximum available period for each dataset to maximize statistical robustness.

3.1 Sub-daily variance decomposition

To quantify the relative contribution of sub-daily (period < 24-hour) variations to the TP variability, a 30th-order Butterworth high-pass filter with a cutoff period of 26 hours (Oppenheim and Schafer, 2010) is applied, separating sub-daily frequency components from relatively lower-frequency components (period ≥ 24-hour, including daily mean), where their respective variance are denoted by σ^2_{subD} and σ^2_{Low} . The mathematical formulation of the sub-daily variance ratio (rat_{subD}) is followed as:

https://doi.org/10.5194/egusphere-2026-2867
Preprint. Discussion started: 3 June 2026

$$rat_{subD} = \frac{\sigma^2_{subD}}{\sigma^2_{total}} \times 100\% \quad (1)$$

where σ^2_{total} is the variance of timely unfiltered time series.

Following Dong et al. (2023) and Covey et al. (2018), σ^2_{subD} is further decomposed into the regular sub-daily variance (σ^2_{reg}), associated with the climatological mean diurnal cycle, and the irregular sub-daily variance (σ^2_{irreg}), representing sub-daily fluctuations that deviate from the climatological mean diurnal cycle on individual days :

$$\sigma^2_{subD} = \sigma^2_{reg} + \sigma^2_{irreg} \quad (2)$$

The regular component is defined as the variance of the climatological mean diurnal cycle P_i^{reg}, obtained by averaging the high-pass filtered precipitation time series over all days at each time of day i:

$$P_i^{reg} = \frac{1}{D}\sum_{n=1}^{D} P_{i,n}, \quad i = 1, \dots, N \quad (3)$$

$$\sigma^2_{reg} = \frac{1}{N}\sum_{i=1}^{N} \left(P_i^{reg} - \overline{P^{reg}}\right)^2 \quad (4)$$

where N is the number of sub-daily time steps per day ($N = 8$ for 3-hourly temporal resolution), D is the total number of days, and $\overline{P^{reg}}$ is the daily mean of P_i^{reg}. The irregular component is obtained as the residual:

$$\sigma^2_{irreg} = \sigma^2_{subD} - \sigma^2_{reg} \quad (5)$$

The regular component is further decomposed into Fourier harmonics via Fast Fourier Transform (FFT). Since P_i^{reg} is a periodic sequence with period N, its variance decomposes as:

$$\sigma^2_{reg} = \sigma^2_{1st} + \sigma^2_{2nd} + \sigma^2_{higher} \quad (6)$$

where σ^2_{1st} and σ^2_{2nd} correspond to the diurnal (24-hour), semidiurnal (12-hour) cycles, respectively, and σ^2_{higher} is the residual variance from higher-order harmonics (period ≤ 8-hour).

3.2 Characterization of regular sub-daily components

UTC-based time coordinates are converted to Local Solar Time (LST; t_{LST}) to explicitly account for the solar forcing of diurnal precipitation (LST=UTC+ $\lambda/15°$, where λ is the longitude in degrees). As 3-hourly time series require an adjustment to align with the discrete time steps, we first calculate $\lambda/45°$, round the result to the nearest integer, and subsequently multiply by 3. This conversion ensures that the diurnal cycle is analysed relative to local solar noon rather than a fixed UTC reference. Such alignment is critical for identifying physically meaningful precipitation phases driven by solar heating.

The sub-daily precipitation is characterized through harmonic analysis, where the precipitation time series are decomposed into Fourier components at each grid point (Cui et al., 2021; Dai, 2001):

https://doi.org/10.5194/egusphere-2026-2867
Preprint. Discussion started: 3 June 2026

$$P(t_{LST}) = \bar{P} + \sum_{k=1}^{N/2} A_k \sin(k\omega t_{LST} + \varphi_k) \quad (7)$$

where $\bar{P}$ is the daily-mean precipitation, A_k and φ_k are the amplitude and phase of the k-th harmonic, N is the number of time sample per day (N = 8 for 3-hourly data), and $\omega = 2\pi/24$. For instance, the 1st harmonic (k = 1, 24-hour period) represents the primary diurnal signal, while the 2nd harmonic (k = 2, 12-hour period) captures semidiurnal variability.

To characterize the relative contribution of individual harmonic components within σ^2_{reg}, (Eq. 6), the fractional contribution of each harmonic component to σ^2_{reg} is defined as:

$$rat_k = \frac{\sigma_k^2}{\sigma^2_{reg}} \times 100\% \quad (8)$$

We quantify the relative dominance of variance at specific frequency bands within the regular sub-daily variability (e.g., 1st (k = 1), 2nd (k = 2), and high-order ($k \geq 3$) harmonics), thereby enabling an assessment of the fidelity of various datasets in capturing the observed spectral balance.

To assess the adequacy of the 1st harmonic component in representing the observed diurnal cycle, we use the rat_1. Regions where $rat_1 \geq 50\%$ indicate that the 24-hour periodic component accounts for at least half of σ^2_{reg}.

3.3 Evaluation of diurnal phase and amplitude

Gridded satellite-based and modelled datasets are evaluated against ground-based observations with respect to the diurnal characteristics of precipitation phase and amplitude. For phase evaluation, we account for the circular nature of the diurnal cycle by calculating the circular mean bias and circular correlation coefficient. The circular mean bias is computed by converting precipitation peak phase into angular values, determining the circular mean difference between the datasets and observation, and subsequently converting the angular difference back to hours. This approach properly resolves periodicity issues–for instance, recognizing that 23:00 LST and 01:00 LST are only 2 hours apart rather than 22 hours. Furthermore, we assess the spatial representation of diurnal phase in the datasets using the circular correlation coefficient (Fisher and Lee, 1994). Its mathematical formulation is followed as:

$$r_c = \frac{\sum_{i=1}^{n} \sin(\theta_i - \bar{\theta}) \sin(\phi_i - \bar{\phi})}{\sqrt{\sum_{i=1}^{n} \sin(\theta_i - \bar{\theta}) \sum_{i=1}^{n} \sin(\phi_i - \bar{\phi})}} \quad (9)$$

where θ and ϕ represent the diurnal phase, expressed by the azimuthal angle (in radians), from the dataset and observations at each grid cell (i) and the overbar represents the circular mean. The circular correlation coefficient ranges from −1 to +1, where values close to +1 indicate robust agreement in the spatial patterns of the diurnal phase. Statistical significance is assessed via the Fisher-Lee test, which approximates the distribution of the circular correlation under the null hypothesis of no association.

https://doi.org/10.5194/egusphere-2026-2867
Preprint. Discussion started: 3 June 2026

For amplitude evaluation, conventional linear statistics are employed, given that amplitude values are non-circular continuous variables. The mean bias is calculated as the arithmetic mean of differences between the dataset and observed amplitudes across all stations, while spatial correlation is quantified using Spearman's rank correlation coefficient. Spearman's method is preferred over Pearson correlation due to its robustness to outliers and independence from linear assumptions, making it particularly appropriate given the high variability of precipitation amplitudes across different climate regimes.

3.4 Atmospheric water budget framework

To elucidate the physical processes underlying the occurrence of diurnal precipitation, the diurnal variations of atmospheric variables controlling moisture availability and convective triggering are examined. Following the atmospheric water budget framework (Song and Wei, 2021), the vertically integrated moisture flux convergence (MFC) is derived as a residual from the water budget equation:

$$MFC = P - E + dPW_t \tag{10}$$

where E is evapotranspiration, P is precipitation, and dPW_t is the tendency of atmospheric precipitable water (PW), estimated as $dPW_t = PW_{t-1} - PW_t$. For the observational reference at the ARM SGP site, E is derived from the latent heat flux of the VARANAL product, P from ARMBEATM, and PW from IGRA version 2 radiosonde observations; for each reanalysis product, the corresponding variables from each dataset are used

MSE is also examined as an integrated measure of the thermodynamic state of the atmosphere. Notably, MSE is considered approximately conserved during adiabatic vertical motions and consists of sensible and latent heat, and geopotential energy, followed as:

$$MSE = C_pT + L_vq + gz \tag{11}$$

where C_p is specific heat at constant pressure, T is temperature, g is gravitational acceleration, z is geopotential height, L_v is the latent heat of vaporization, and q is specific humidity. MSE is computed over the range 925–400 hPa, effectively representing the thermodynamic conditions of the lower-to-middle troposphere essential for convective triggering.

https://doi.org/10.5194/egusphere-2026-2867
Preprint. Discussion started: 3 June 2026

4 Results

4.1 Precipitation variability in sub-daily time scales

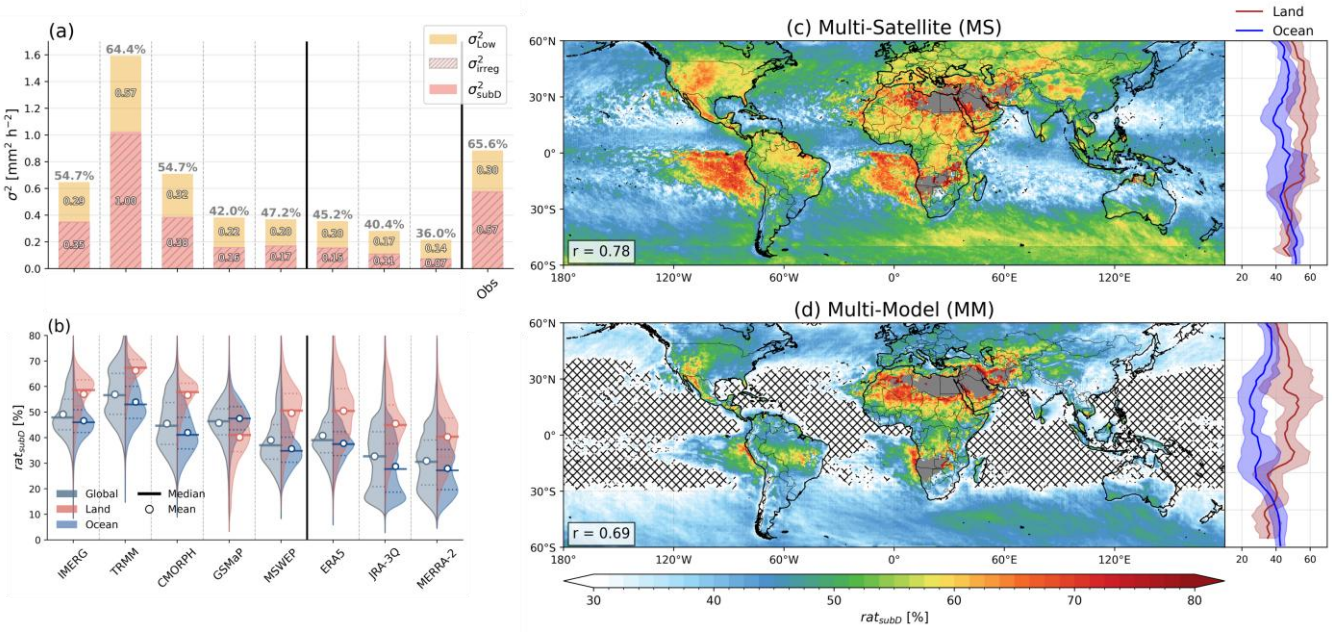

Figure 3: (a) Sub-daily frequency (pink) and lower-frequency (orange) variance components of precipitation at observation locations. Sub-daily frequency variance is obtained via high-pass Butterworth filter. Numbers inside bars indicate variance magnitude mm² h⁻², and percentage above bars represent the Sub-daily variance ratio (rat_{subD}). (b) Violin plots of the rat_{subD} distribution for each dataset over the globe (black, left side), land (red, right side), and ocean (blue, right side), where the thick solid line and circle indicate the median and mean, respectively, and dashed lines denote the 25th and 75th percentiles. Spatial distribution of rat_{subD} from (c) Multi-Satellite (IMERG, TRMM, CMORPH, GSMaP, MSWEP) mean and (d) Multi-Model (ERA5, JRA-3Q, MERRA-2) mean, where crossed areas indicate rat_{subD} is below 30%. The spatial correlation of both products against ground-based observations is denoted in the lower left of each panel. The zonal averaged distribution over the land (red) and ocean (blue) is displayed on the right of each panel and shading represents ±1 standard deviation.

The characteristics of precipitation have been extensively investigated across various temporal scales, including interannual, seasonal, daily, and diurnal cycles. However, the importance of high-frequency variability, particularly at sub-daily scales, has received less emphasis compared to lower-frequency domains. While some studies have explored high-frequency precipitation variability using remotely sensed and modelled products, comprehensive evaluations and comparisons with ground-based observations on a continental scale remain limited. Total variance of precipitation at observational sites during boreal summer is 0.9 mm² h⁻², whereas most of precipitation datasets represent the underestimated variance, and the underestimation is more apparent in the reanalysis products. In contrast, TRMM overestimates the variance, as its onboard Precipitation Radar is more sensitive to moderate-to-heavy CP while under sampling light precipitation events (Rasmussen et al., 2014). The underestimation of total variance is primarily attributed to the underestimated σ^2_{subD} despite the underestimation of σ^2_{Low}. For instance, while σ^2_{Low} from satellite-based datasets is comparable to observations, they generally underestimate σ^2_{subD}, with the notable exception of TRMM. For reanalysis products, ERA5 reproduces only 64% of the observed σ^2_{Low} and a

https://doi.org/10.5194/egusphere-2026-2867
Preprint. Discussion started: 3 June 2026

mere 28% of the observed σ^2_{subD}. In contrast, MERRA-2 exhibits the most substantial underestimation, capturing only 46% of the observed σ^2_{Low} and 13% of the σ^2_{subD} relative to observations.

Further decomposing σ^2_{subD} into regular (σ^2_{reg}) and irregular (σ^2_{irreg}) components provides additional insight into the source of this underestimation. In observations, σ^2_{irreg} accounts for approximately 98% of σ^2_{subD}, indicating that the repeatable diurnal signal is overwhelmed by day-to-day variability in sub-daily precipitation. While convective intermittency and irregular occurrence of MCSs are likely dominant contributors over land (Covey et al., 2018), other sources (e.g., synoptic-scale forcing variability) also project onto σ^2_{irreg}. σ^2_{reg} also exhibits considerable deviation from observations across all datasets. Notably, despite the more severe underestimation of σ^2_{irreg} in reanalysis products relative to satellite-based datasets, the relative contribution of σ^2_{reg} within σ^2_{subD} is overestimated in reanalysis products (5–8%) than in satellite-based datasets (2–3%). The disparity in underestimation between σ^2_{Low} and σ^2_{subD}, and particularly the underrepresentation of σ^2_{irreg}, is primarily attributed to two factors. First, satellite-based datasets, where gauge-based observations are typically assimilated to correct relatively low-frequency variations (e.g., daily, pentad, and monthly), leave sub-daily scales less constrained. Second, for reanalysis products, the underestimation of σ^2_{subD} is further exacerbated by the inherent limitations of parameterization schemes in capturing precipitation physics at relatively coarse spatial resolutions (Herold et al., 2016; Skok et al., 2016). These constraints lead to an excessive frequency of light precipitation, which hinders the simulation of intense rainfall during sub-daily time scales (Chen et al., 1996; Dai, 2006a; Stephens et al., 2010).

The observed rat_{subD}, quantifying the relative contribution of sub-daily precipitation variability against its total variance, exhibits that 65.6% of total variance is explained by both systematic diurnal and irregular high-frequency fluctuations. This result serves as a benchmark for evaluating whether datasets accurately reproduce the temporal partitioning of precipitation variability. All satellite-based and reanalysis datasets underestimate the observed rat_{subD}, with modeled products consistently falling below 50% of the observed value (ERA5: 45.2%, JRA-3Q: 40.4%, MERRA-2: 36.0%). Regarding the land-ocean contrast, rat_{subD} over land exceeds that over the ocean in most datasets (Fig. 3b). Most land regions exhibit relatively strong sub-daily precipitation variability relative to the ocean, reflecting greater intensity and frequency of convective precipitation events over land (Li et al., 2025). The lower tail of the negatively skewed distribution corresponds to areas where large-scale dynamics or orographic effects suppress typical diurnal signals. Conversely, oceanic distributions are positively skewed, indicating that while most regions exhibit low rat_{subD} values reflecting the relatively larger contribution of day-to-day precipitation variability to total variance over the ocean (Covey et al., 2018), the upper tail corresponds to specific areas where reduced low-frequency variability yields disproportionately high sub-daily fractions. GSMaP stands out as a notable exception, exhibiting a reversed land–ocean contrast in rat_{subD} with a lower median over land than over ocean. This may stem from a combination of two land-specific characteristics of the GSMaP retrieval and calibration system. First, GSMaP is known to exhibit a systematic intensity-dependent bias over land, which overestimates light precipitation frequency while underestimating heavy precipitation intensity (Chen et al., 2019; Ning et al., 2017; Pradhan et al., 2025). It suppresses the

https://doi.org/10.5194/egusphere-2026-2867
Preprint. Discussion started: 3 June 2026

physical amplitude of both the regular diurnal cycle and the episodic high-frequency fluctuations relative to other satellite products. Second, GSMaP is applied exclusively over land and uniformly scales hourly precipitation rates to match daily CPC gauge totals (Mega et al., 2019), a process that directly modifies the absolute values of hourly precipitation over land while leaving ocean sub-daily variance unconstrained. In contrast, IMERG applies a temporally fixed monthly ratio that leaves sub-daily structure intact (Huffman et al., 2023), and CMORPH adjusts distributional shape through probability density function matching without constraining hourly magnitudes (Xie et al., 2017).

The rat_{subD} spatial patterns from Multi-Satellite (MS) and Multi-Model (MM) mean reveal distinct regional characteristics (Figs. 3c, d). Both product suites represent the pronounced geographic pattern of strong sub-daily variability in land regions where rat_{subD} reaches approximately 50%. The reanalysis products exhibit globally lower rat_{subD} compared to satellite-based datasets, particularly pronounced over the ocean. In the zonally averaged distribution, satellite-based products show relatively uniform rat_{subD} meridionally both land and ocean areas. In contrast, the modelled distribution displays a pronounced meridional gradient, characterized by distinct disparities between land and ocean, particularly in the tropics. In terms of spatial agreement with ground-based observations over NH land, the MS demonstrates superior performance over the MM, as evidenced by its higher spatial correlation (Δr=0.09).

https://doi.org/10.5194/egusphere-2026-2867
Preprint. Discussion started: 3 June 2026

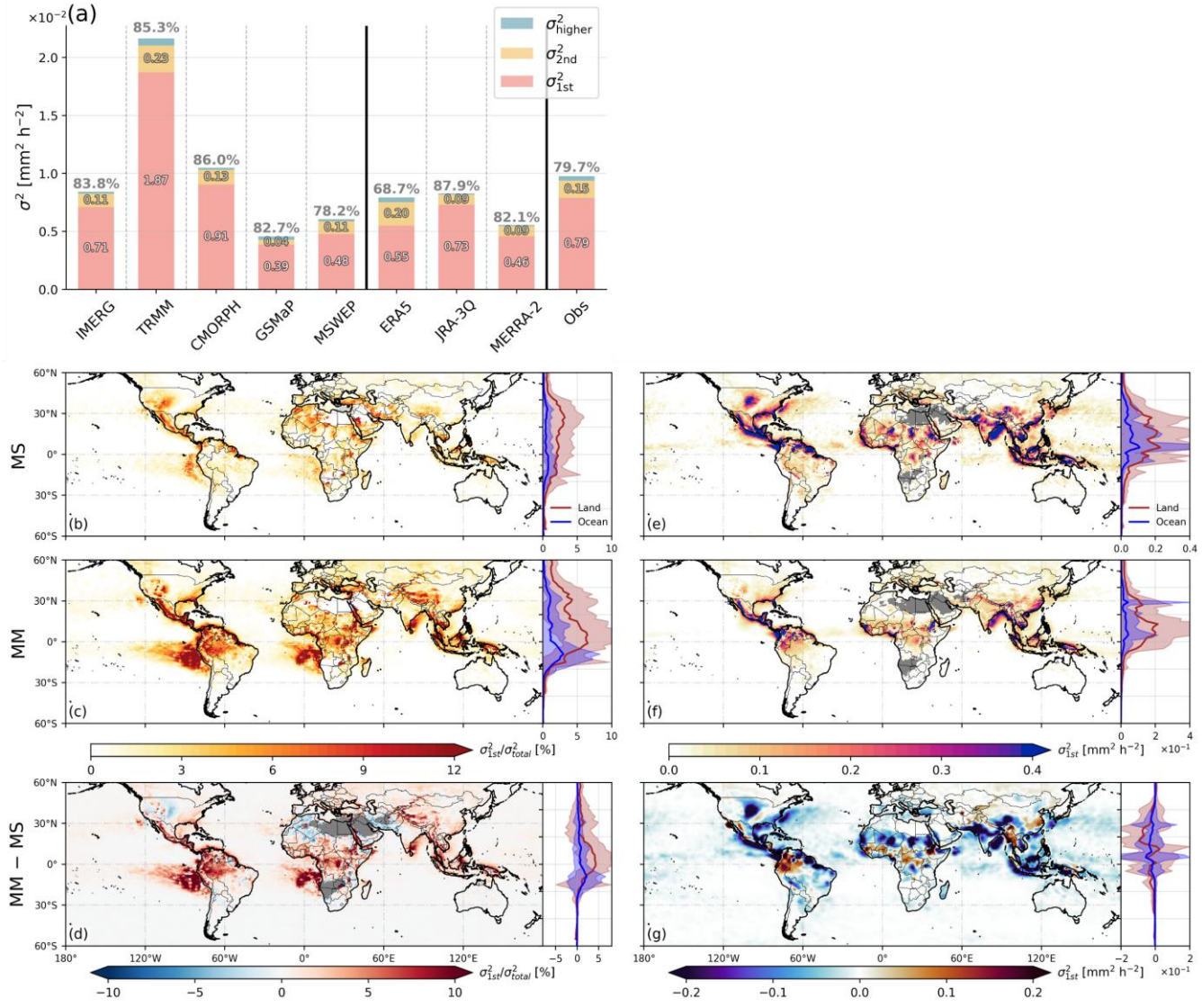

Figure 4: (a) Same as Fig.3a, but for regular sub-daily precipitation variance (σ^2_{reg}) decomposed into the 1st (pink), 2nd (orange), and higher-order (blue) harmonic components. Numbers within bars indicate the variance magnitude (mm^2 h^{-2}), and percentage above bars represent the fraction of the 1st harmonic within $\sigma^2_{reg}(rat_1)$. (b,c,d) Spatial distributions of $\sigma^2_{1st}/\sigma^2_{total}$ and (e,f,g) σ^2_{1st} from (b, e) Multi-Satellite (IMERG, TRMM, CMORPH, GSMaP, MSWEP) mean, (c, f) Multi-Model (ERA5, JRA-3Q, MERRA-2) mean, and (d, g) their difference (MM-MS). The zonal mean distribution over the land (red) and ocean (blue) is displayed on the right of each panel, where the shading represents ±1 standard deviation.

Although σ^2_{irreg} dominates σ^2_{subD} across all datasets (Fig. 3a), the regular component σ^2_{reg} is of particular diagnostic value as it encodes the physically interpretable periodic structure of sub-daily precipitation variability (including the diurnal and semi-diurnal cycles that are directly linked to surface thermal forcing, boundary layer dynamics, and atmospheric tides). The absolute magnitude of each harmonic component of σ^2_{reg} reveals more pronounced differences than the composition ratios

https://doi.org/10.5194/egusphere-2026-2867
Preprint. Discussion started: 3 June 2026

(Fig. 4a), with CMORPH (0.0091 mm^2 h^{-2}) showing the closest agreement with observations (0.0079 mm^2 h^{-2}) among satellite based products. Reanalysis products generally show smaller absolute values of σ_{1st}^2 relative to observations, with MERRA-2 exhibiting the lowest value (0.0046 mm^2 h^{-2}). ERA5 shows a notably larger contribution of σ_{2nd}^2 relative to other datasets.

The magnitude of $\sigma_{1st}^2/\sigma_{total}^2$ in MS (Fig. 4b) peaks around 30°N over continental regions, with prominent values over central North America, India, southern China, and interior Africa, whereas the over ocean it is generally lower. In contrast to rat_{subD} (Figs. 3c, d), MM shows generally larger $\sigma_{1st}^2/\sigma_{total}^2$ than the MS (Fig. 4c), with values exceeding 10% near the equatorial land and decreasing poleward before increasing again around 30°N. This arises from the severe underrepresentation of σ_{irreg}^2 (cf., Fig. 3a), which reduces σ_{total}^2 disproportionately and thereby inflates the relative contribution of σ_{1st}^2.

The spatial distributions of σ_{1st}^2 (Figs. 4e, f) show maximum values over 0–30°N continental regions in both product suites, with particularly prominent signals over southern China, the Amazon, the GP, and the Maritime Continent. The MM (Fig. 4f) consistently underrepresents σ_{1st}^2 over both land and ocean, reflecting the characteristic of reanalysis products wherein the relative contribution of σ_{reg}^2 within σ_{subD}^2 is overestimated while its absolute magnitude is underrepresented. This underrepresentation of σ_{reg}^2 is not confined to reanalysis products; satellite-based datasets such as GSMaP and MSWEP also exhibit notably lower absolute values relative to observations, suggesting that the physical intensity of the regular diurnal cycle component remains challenging across multiple product types.

On the other hand, the difference between MS and MM in both $\sigma_{1st}^2/\sigma_{total}^2$ (Fig. 4d) and σ_{1st}^2 (Fig. 4g) reveals that the origin of this overestimation varies by region. For instance, over the western coast of Chile and southern Africa, the MM overestimates $\sigma_{1st}^2/\sigma_{total}^2$ despite negligible differences in σ_{1st}^2 itself, indicating that the inflated ratio stems from a reduction in σ_{total}^2 driven by the underrepresentation of σ_{irreg}^2 rather than from errors in the diurnal cycle amplitude. Over the eastern coast of India, the Maritime Continent, and tropical continental interiors, the MM simultaneously overestimates $\sigma_{1st}^2/\sigma_{total}^2$ while underestimating σ_{1st}^2, implying that the far more severe underrepresentation of σ_{irreg}^2 reduces σ_{total}^2 to a greater extent than the reduction in σ_{1st}^2. In contrast, over the GP and northwestern India, both $\sigma_{1st}^2/\sigma_{total}^2$ and σ_{1st}^2 are underestimated by the MM, suggesting that in these regions the insufficient physical intensity of the diurnal cycle itself is the dominant source of error, rather than the underrepresentation of σ_{irreg}^2.

https://doi.org/10.5194/egusphere-2026-2867
Preprint. Discussion started: 3 June 2026

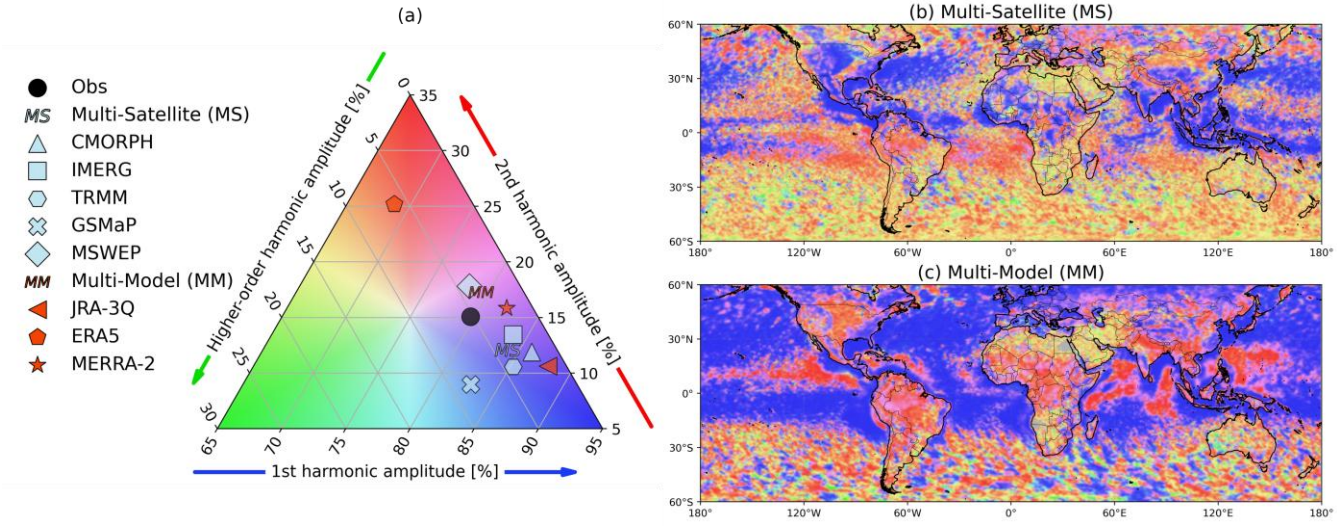

Figure 5: (a) Ternary diagram of harmonic amplitude ratios for 1st (bottom axis), 2nd (right axis), and higher-order (left axis) harmonic components of regular sub-daily precipitation variability, where the averaged value from each dataset over grid cells collocated with ground-based observations is marked by a distinct symbol. Shading colour in (a) defines the colour scale used in the spatial distributions of harmonic balance from (b) Multi-Satellite and (c) Multi-Model mean.

To characterize the temporal frequency distribution of regular sub-daily precipitation variability (σ^2_{reg}), the relative contributions of various harmonic components are examined via power spectrum analysis. Ground-based observations show a 1st harmonic (24-hour period) fraction of 79.7%, a 2nd harmonic fraction of 15.1%, and higher-order contributions of 5.0% (Fig. 5a). Satellite-based products generally overestimate the contribution of the 1st harmonic relative to observations (MS: 84.1%), with CMORPH (86.0%) and TRMM (85.3%) exhibiting a pronounced overestimation alongside a corresponding underestimation of the 2nd harmonic. Among individual satellite products, MSWEP (78.2%) captures the observed 1st harmonic fraction well, while also demonstrating superior performance in representing mean climatology (Dirmeyer et al., 2018), suggesting that its multi-source merging approach provides reliable performance across multiple timescales. Within reanalysis products, ERA5 exhibits the lowest 1st harmonic dominance (68.7%) and the highest 2nd harmonic fraction (25.2%) of all evaluated datasets, whereas JRA-3Q (87.9%) presents the most substantial overestimation of the 1st harmonic. While the MM mean (79.4%) appears numerically closest to observations, this results from the mutual cancellation of ERA5's 2nd harmonic excess and JRA-3Q's 1st harmonic overestimation; therefore, it reflects a statistical artifact rather than a physically consistent reproduction of the observed harmonic balance.

The spatial distribution of harmonic amplitude ratios in MS (Fig. 5b) indicates that the 1st harmonic dominates over major continental interiors, including the North American Great Plains, India, central Africa, and southeastern China, as well as over midlatitude oceans and continental eastern coasts. Over high-latitude oceans and some subtropical arid regions, no harmonic component exhibits clear dominance, producing irregular patterns that likely reflect insufficient precipitation frequency for stable harmonic decomposition. In contrast, reanalysis products show smaller 1st harmonic amplitudes over major continental interiors compared to the satellite-based retrievals, with correspondingly larger contributions from the 2nd harmonics (Fig. 5c),

https://doi.org/10.5194/egusphere-2026-2867
Preprint. Discussion started: 3 June 2026

reflecting the inability of reanalysis convective parameterization to reproduce the observed thermally driven diurnal cycle (Dai, 2024; Tang et al., 2021). The amplified semi-diurnal component in reanalysis products does not reflect a superior representation of physical processes; instead, it indicates the spurious generation of semi-diurnal precipitation variability inherent in model parameterization schemes. Over most ocean basins, the MM exhibits broadly uniform 1st harmonic dominance, including tropical and subtropical regions where the MS displays heterogeneous harmonic compositions. At high latitudes, the MM maintains a comparatively uniform 1st harmonic dominance, contrasting sharply with the spatially incoherent harmonic patterns seen in the MS. This discrepancy between MS and MM is particularly evident over the western Pacific Monsoon Trough, where the 2nd harmonic contribution in the MM exceeds 30%, whereas the MS exhibits spatially noisy patterns that preclude a clear assessment of harmonic dominance in this region.

4.2 Diurnal cycle patterns and underlying mechanisms

https://doi.org/10.5194/egusphere-2026-2867
Preprint. Discussion started: 3 June 2026

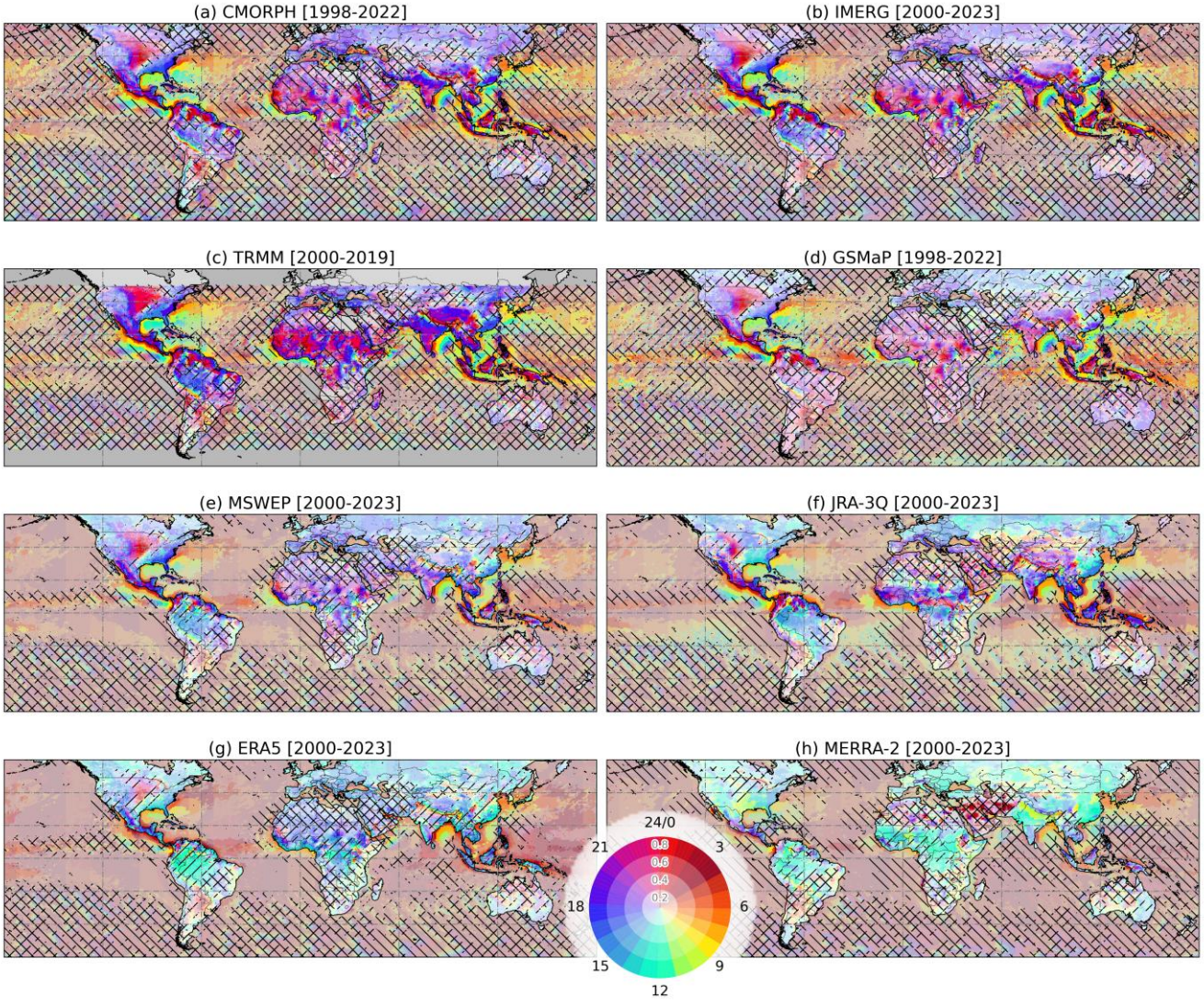

Figure 6: Global maps of diurnal phase (colour) and amplitude (colour intensity) of precipitation from (a) CMORPH, (b) IMERG, (c) TRMM, (d) GSMaP, (e) MSWEP, (f) JRA-3Q, (g) ERA5 and (h) MERRA-2. Backward (\) slashed area denotes regions where daily precipitation amount is less than 0.275 mm or normalized amplitude of diurnal cycle < 30% (Watters et al., 2021), and forward (/) slash indicates areas where rat_1 is less than 50%. NARR is not shown in the global map as it covers only the North American domain (10°N–85°N, 140°W–60°W) and is evaluated separately in Fig. 7b.

Satellite-based datasets consistently capture a pronounced land–ocean contrast in the diurnal phase of precipitation (Figs. 6a–e). Across most tropical, subtropical, and mid-latitude land regions, precipitation predominantly peaks during the late afternoon to evening (15–21 LST). In contrast, nocturnal to early-morning maxima (21–06 LST) are evident over the U.S. GP, parts of the Amazon Basin, central Africa, and the eastern periphery of the Tibetan Plateau. These patterns are underpinned by nocturnal precipitation regimes associated with LLJ activity and propagating MCSs. Over the oceans, precipitation manifests a distinctly different temporal signature, with peaks occurring during the early morning (03–09 LST), consistent with the

https://doi.org/10.5194/egusphere-2026-2867
Preprint. Discussion started: 3 June 2026

nocturnal destabilization of the marine boundary layer driven by radiative cooling aloft (Gray and Jacobson, 1977). Furthermore, the diurnal amplitude exhibits significant spatial heterogeneity, with the most robust variations observed over land, while oceanic regions are characterized by damped amplitudes due to minimal surface diurnal temperature fluctuations. Along coastal regions, intermediate phases (06–12 LST) emerge between the land and oceanic regimes, reflecting the offshore propagation of convective systems initiated over land. This coastal-to-inland phase transition is particularly pronounced over the maritime continent, western India, West Africa, and the Atlantic coast of South America, and is well captured by CMORPH and IMERG.

Distinct disparities exist among the satellite products; for instance, CMORPH and IMERG demonstrate the highest degree of spatial consistency in both phase and amplitude. This similarity is rooted in their shared morphing framework, as the IMERG integration algorithm directly leverages the CMORPH Kalman filter-based morphing technique to propagate PMW retrievals across time and space (Huffman et al., 2020; Xie et al., 2017). Pradhan et al. (2025) similarly reported that IMERG and CMORPH produce the most similar diurnal patterns among evaluated satellite products in K-means cluster analysis. TRMM exhibits notably greater amplitudes than other satellite products, consistent with the elevated sub-daily variance discussed in Section 4.1 (Fig. 3a). GSMaP shows broadly consistent spatial pattern over land with other satellite products, but exhibits notable differences over tropical oceans, including more extensive areas of early morning precipitation maximum (03–06 LST) and weaker amplitude over land regions. Additionally, the nocturnal propagation signal associated with organized convective systems over tropical ocean is less pronounced in GSMaP compared to IMERG and CMORPH. MSWEP displays spatially smoother patterns and systematically earlier precipitation peak (approximately 15 LST) compared to other satellite products, attributable to the use of ERA5 reanalysis for its sub-daily temporal disaggregation, which introduces the early precipitation bias inherent in reanalysis products.

Reanalysis datasets exhibit systematic premature phase bias over land relative to satellite products. In contrast, they demonstrate higher fidelity over the ocean, with early-morning peaks (03–06 LST) that align well with observations (Figs. 6f–h). It has been commonly reported in evaluations of CMIP models and reanalysis datasets (Tang et al., 2021; Watters et al., 2021), and is associated with convective parameterization schemes triggering precipitation too rapidly in response to solar heating over land, whereas radiatively driven oceanic precipitation timing is more realistically reproduced (Dai and Trenberth, 2004). The magnitude of phase shift over land varies among reanalysis products. JRA-3Q shows relatively consistent spatial patterns with satellites (Fig. 6f), exhibiting afternoon precipitation peak (approximately 14–18 LST) over most continental regions. Notably, JRA-3Q partially captures the observed spatial transition associated with nocturnal precipitation propagation over the U.S. GP and North China Plain. In contrast, ERA5 exhibits more pronounced phase offsets (Fig. 6g), with diurnal peaks occurring between midday and early afternoon (12–15 LST) over tropical landmasses, such as South America, Africa, and Southeast Asia. Although ERA5 shows some indications of nocturnal propagation near mountainous terrain, its spatial coherence is considerably weaker than that of JRA-3Q. MERRA-2 displays the most significant phase discrepancies (Fig. 6h), with precipitation peaking uniformly during the late morning (09–12 LST). Unlike other products, MERRA-2 fails to resolve

https://doi.org/10.5194/egusphere-2026-2867
Preprint. Discussion started: 3 June 2026

regional phase variations, such as the nocturnal maxima over mountains and afternoon peaks over continental interiors, resulting in a spatially invariant phase distribution. Regarding the diurnal amplitude, reanalysis products generally underestimate the magnitudes observed in satellite-based datasets.

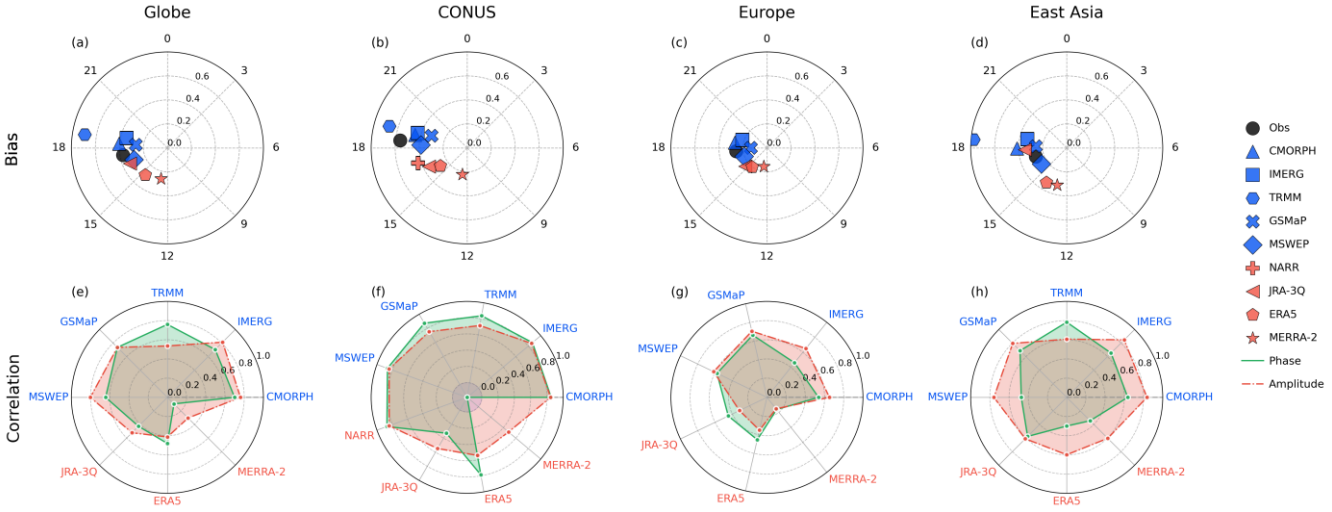

Figure 7: Spatially averaged diurnal phase (azimuth) and amplitude (radius) of the precipitation from ground-based observation (black), satellite (blue), and reanalysis (red) datasets over (a) the globe, (b) Contiguous United States (CONUS), (c) Europe (EU), and (d) East Asia (EA), for grid points where $rat_1 \geq 50\%$. (e-h) The spatial correlation of diurnal phase (green solid) and amplitude (red dashed) from gridded products with the observation is denoted below row.

The quantitative analysis of diurnal phase and amplitude corroborates the inter-dataset discrepancies identified qualitatively in Fig. 6. While ground-based observations indicate a peak phase at approximately 17 LST, most satellite products, despite capturing the general timing, exhibit a systematic temporal lag of approximately 1–2 hours (Fig. 7a). This systematic delay arises from the indirect detection characteristics inherent in satellite precipitation retrieval algorithms. PMW sensors detect hydrometeors at ice-scattering altitudes in the upper troposphere rather than at the surface, and preferentially capture CP more effectively than stratiform precipitation (Ebert et al., 2007; Hayden and Liu, 2021). Furthermore, the extensive anvil regions of organized convective systems can continue expanding after surface precipitation reaches its maximum and persist even after the convective core dissipates, such that PMW sensors still detect strong ice-scattering signals during phases when surface precipitation has already weakened. TRMM exhibits comparable phasing to other satellite products but with approximately twice the amplitude, a direct consequence of the elevated sub-daily variance identified in Fig. 3. MSWEP displays a phase of approximately 16 LST, roughly 1 hour earlier than observations. Reanalysis products exhibit systematic premature phase biases and attenuated amplitudes. Specifically, the magnitude of this phase lead increases progressively across the datasets, with peak precipitation timing shifting from 16 LST in JRA-3Q to 14 LST in ERA5, reaching 12 LST in MERRA-2.

The diurnal cycle of precipitation exhibits distinct regional characteristics. Over CONUS, where the peak diurnal phase is observed at 18 LST, satellite products generally capture the observed timing but tend to underestimate the robust diurnal

https://doi.org/10.5194/egusphere-2026-2867
Preprint. Discussion started: 3 June 2026

amplitude (Fig. 7b). While most reanalysis products highlight the persistent challenges in simulating diurnal precipitation over this region, NARR demonstrates superior fidelity in reproducing both the observed phase and amplitude. This performance is directly attributable to its 3-hourly assimilation of precipitation observations, thereby underscoring the efficacy of precipitation data assimilation in accurately representing diurnal cycle dynamics.

The observed diurnal phases in Europe (EU) and East Asia (EA) occur around 16–17 LST, with magnitudes that are comparable between the two regions yet notably smaller than those over CONUS (Figs. 7c, d). These subdued amplitudes are consistent with the lower rat_{subD} values observed in the EU (50–60%) and EA (30–50%) compared to CONUS (70–80%). This suggests that synoptic-scale and lower-frequency variability account for a greater proportion of the TP variance in these regions. However, the physical mechanisms underlying the weak diurnal amplitudes differ between the two regions. Over the EU, summertime frontal and orographic precipitation contributes significantly to the total rainfall, whereas the thermally driven convective diurnal signal remains relatively weak. In EA, synoptic-scale systems, such as the Meiyu/Baiu/Changma frontal zones associated with the East Asia summer monsoon, account for a substantial portion of the precipitation variability. Despite the EA exhibiting lower rat_{subD} than the EU, the two regions manifest similar diurnal amplitudes. This likely reflects the larger σ^2_{total} in the EA driven by synoptic environments, while the activation of nocturnal low-level jets partially sustains the diurnal signal even within LSP systems (Yu et al., 2007).

We further evaluate the spatial consistency of the diurnal phase and amplitude between gridded products and observations (Figs. 7e–h). Regarding the diurnal phase, satellite products achieve the strongest correlations over the CONUS ($r > 0.8$), with moderate agreement over EA (r = 0.5–0.7) and the weakest performance over the EU. The complex topography and the coexistence of diverse precipitation mechanisms (e.g., frontal, orographic, and convective) in the EU and EA induce higher spatial variability, complicating the representation of the diurnal phase. Overall, the performance of reanalysis products is inferior to that of satellite datasets. Across the globe, CONUS, and EU, ERA5 shows comparable or higher phase correlations than JRA-3Q; however, JRA-3Q remains the most reliable reanalysis for capturing the observed diurnal patterns. A notable exception occurs in the diurnal amplitude over EA (Fig. 7h), where most datasets (excluding TRMM) yield correlation coefficients approximately 0.2 higher than their respective phase correlations. This suggests that the spatial distribution of amplitude is more consistently reproduced across various datasets than the phase.

https://doi.org/10.5194/egusphere-2026-2867
Preprint. Discussion started: 3 June 2026

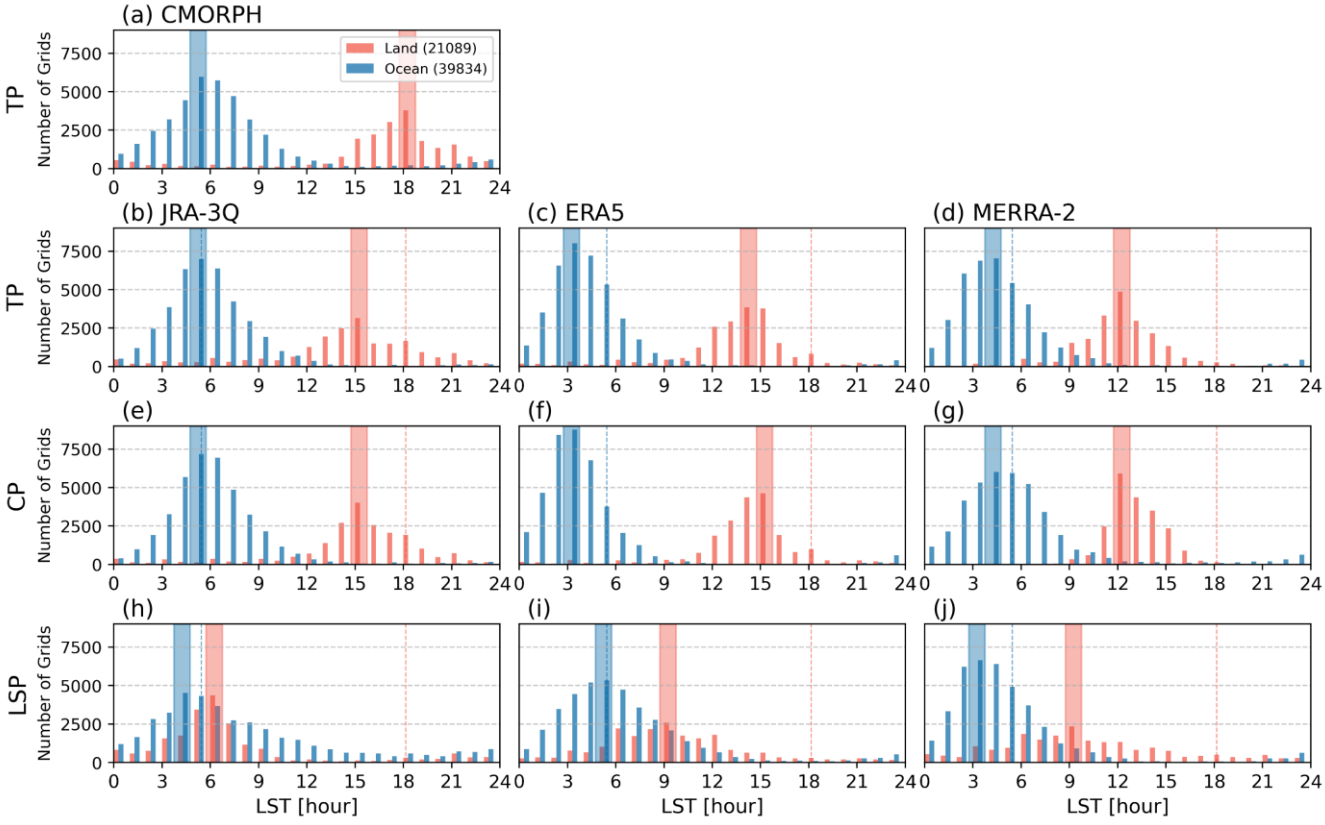

Figure 8: Histograms of the frequency distribution of the diurnal peak phase for total (left column, TP), convective (middle column, CP), and large-scale (right column, LSP) precipitation over land (red) and ocean (blue) grids bounded by 60°S–60°N (only grid point after backward and forward masking in Fig. 6) from (a) CMORPH, (b, e, h) JRA-3Q, (c, f, i) ERA5, and (d, g, j) MERRA-2. Background shaded bars indicate the local time corresponding to the maximum frequency of grid points for the diurnal peak phase.

To elucidate the physical processes underlying these phase shifts, we examine the respective contributions of different precipitation types to the TP diurnal cycle. The diurnal phase of precipitation exhibits systematic differences according to precipitation type, which can be quantified by separately analysing the peak phase distributions for TP, CP, and LSP (Fig. 7). Unlike CMORPH, which provides only TP, reanalysis datasets partition precipitation into convective and large-scale components via their respective parameterization schemes. This partitioning enables a detailed investigation into the physical mechanisms responsible for diurnal phase biases. Specifically, this decomposition is instrumental in determining whether these phase errors originate from convective triggering mechanisms, stratiform precipitation processes, or the complex interplay between the two processes.

TP from CMORPH exhibits divergent peak distributions between land and ocean (Fig. 8a). Over land, the peak phase distribution shows a broad maximum centred around 18 LST, reflecting the dominance of afternoon convection driven by surface heating. Most terrestrial grid points peak between 15 and 21 LST; however, a secondary peak is also evident during

https://doi.org/10.5194/egusphere-2026-2867
Preprint. Discussion started: 3 June 2026

the late evening (21 LST), representing regions influenced by nocturnal MCSs, such as the central U.S. GP and parts of South America. In contrast, the oceanic precipitation peak is more pronounced in the early morning, specifically at 05 LST.

Reanalysis TP over land (Fig. 8b–d) consistently exhibits a diurnal early peak compared to CMORPH, although the magnitude of this phase shift varies among products. JRA-3Q displays the smallest shift with a peak at approximately 15 LST (~3 hours early), while ERA5 peaks at 14 LST and MERRA-2 at 12 LST. Over the ocean, all three reanalysis products show early-morning peaks (03–06 LST) that are consistent with CMORPH, indicating that the diurnal early phase bias is predominantly a terrestrial phenomenon. The decomposition of precipitation types reveals that TP peak phase in all reanalysis products aligns closely with the CP peak phase over land (Fig. 8e–j). In contrast, LSP consistently peaks during the morning over land, which clearly decoupled from TP and CP phases. The LSP morning maximum broadens the TP distribution but does not determine the TP peak timing itself.

Although all reanalysis products exhibit this CP-dominated diurnal cycle, notable discrepancies exist regarding the relative partitioning between CP and LSP. In JRA-3Q and ERA5, the frequency of CP peaks exceeds that of LSP across both land and oceanic domains, indicating that the convective component governs the diurnal phase of precipitation. MERRA-2, however, displays a unique oceanic partitioning where the LSP peak frequency (Fig. 8j) markedly surpasses the CP peak frequency (Fig. 8g), contrasting with the CP-dominant partitioning in JRA-3Q and ERA5. This LSP-dominant oceanic precipitation in MERRA-2 aligns with the documented tendency of the Relaxed Arakawa–Schubert (RAS) scheme, particularly when utilizing a Tokioka-type trigger, to suppress deep convective activity (Bacmeister and Stephens, 2011; Gelaro et al., 2017). This suppression consequently leads to reduced CP intensity compared to other reanalysis products (Tao et al., 2024). Furthermore, the diurnal peak phase of LSP in MERRA-2 is at 09–12 LST (Fig. 8j), overlapping in phase with its CP maximum, unlike the clearly separated morning LSP peaks in JRA-3Q and ERA5. Such phase alignment suggests that convective processes in MERRA-2 may be inadvertently represented through the large-scale condensation scheme instead of the convective parameterization.

The decomposition of precipitation types thus provides direct evidence that premature convective triggering, rather than LSP processes, serves as the primary driver of systematic early peaks in reanalysis TP. This finding corroborates previous studies that identify convective parameterization as the fundamental source of diurnal phase shift (Dirmeyer et al., 2012). To further elucidate the thermodynamic and moisture budget processes underlying these convective phase biases, the following section examines the diurnal evolution of CAPE, MFC, and other related atmospheric variables.

4.3 Physical mechanisms of the diurnal cycle

https://doi.org/10.5194/egusphere-2026-2867
Preprint. Discussion started: 3 June 2026

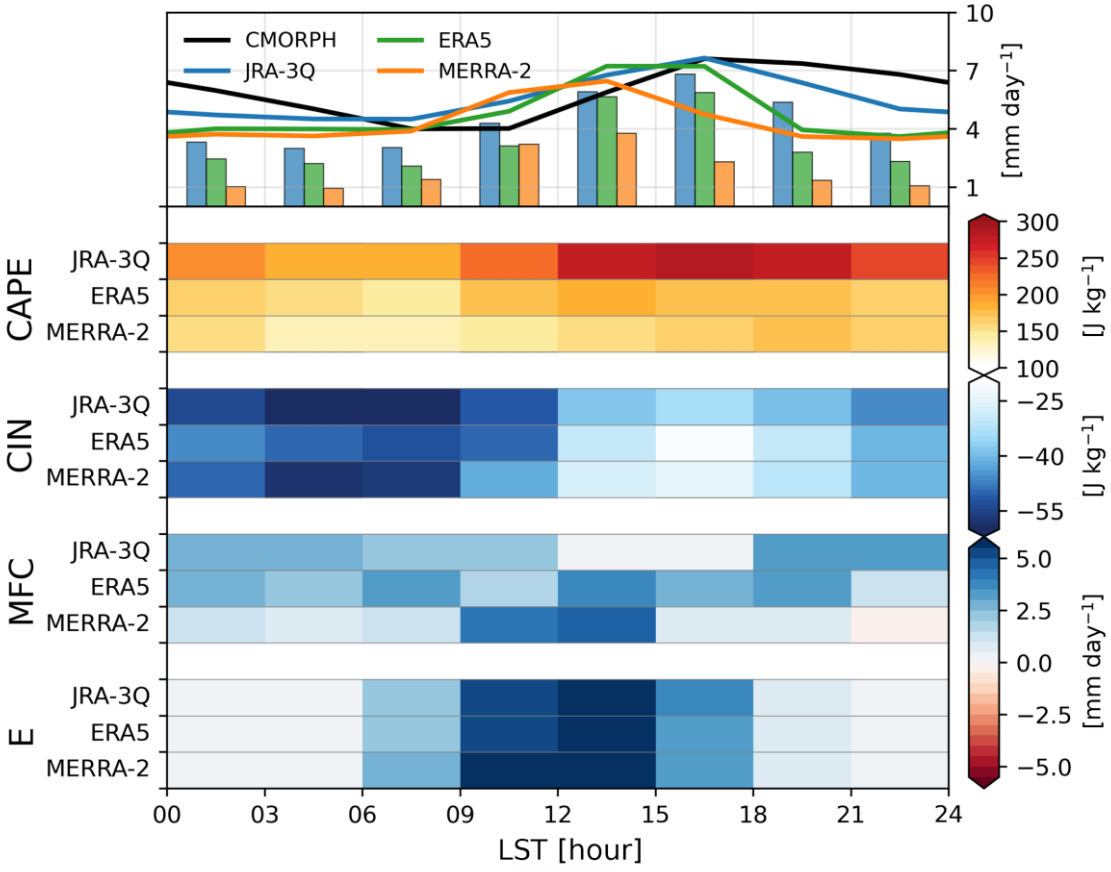

Figure 9: Diurnal cycle of area-averaged precipitation and its relevant variables for rainy days (daily precipitation ≥ 0.275 mm day⁻¹) over 0°–60°N. Upper panel shows the diurnal cycle of TP (lines) and CP (solid bars) from CMORPH, JRA-3Q, ERA5, and MERRA-2. Lower panels show diurnal variations of CAPE, CIN, MFC, and E, where each row represents three reanalysis datasets (JRA-3Q, ERA5, and MERRA-2).

To understand the underlying physical processes responsible for the systematic phase shift identified previously, we examine the diurnal evolution of key variables related to precipitation occurrence, including CAPE, CIN, MFC, and E (Fig. 9). This analysis focuses on rainy days (daily precipitation ≥ 0.275 mm day^{-1}) over the Northern Hemisphere (0°–60°N) during the boreal summer season. The interrelationships among these variables reveal fundamental differences in how various reanalysis parameterization schemes couple surface processes, boundary layer dynamics, and free-tropospheric forcing to modulate precipitation development. The observed precipitation reaches its diurnal peak phase between 15 and 18 LST, which is consistent with the well-established 3–6 hours lag following maximum surface heating. This characteristic delay reflects the time required for boundary layer moisture accumulation, the progressive erosion of CIN, and the subsequent transition from shallow to deep convection (Dai et al., 1999; Stirling and Stratton, 2012; Tian and Kuang, 2016).

The diurnal cycle of TP in the reanalysis datasets confirms the premature phase lead identified in the previous subsection. In all three products, the rise in CP closely tracks the TP rise, reinforcing the dominance of the convective component. *E*

https://doi.org/10.5194/egusphere-2026-2867
Preprint. Discussion started: 3 June 2026

exhibits the most consistent diurnal pattern across all three reanalysis products, with a peak occurring between 09 and 15 LST in each case. This consistency suggests that the supply of surface moisture to the boundary layer, which is an essential precursor for convective development through CAPE accumulation and CIN erosion (Dai, 2024), does not vary substantially among the products. Consequently, the discrepancies in the precipitation peak phase are not primarily attributed to the surface forcing itself, but rather to how each convective parameterization scheme responds to the resulting destabilization. In CMORPH, the characteristic 3–6 hours lag between peak surface fluxes and the diurnal precipitation maximum reflects the finite time required for the aforementioned processes. The extent to which each reanalysis product reproduces this delay is fundamentally governed by its specific convective triggering mechanism.

The relationship between CAPE and precipitation elucidates fundamental differences in convective triggering behaviour. In JRA-3Q, CAPE increases gradually after sunrise and reaches its maximum at 15–18 LST (approximately 350 J kg^{-1}), while precipitation peaks at roughly 15 LST, coinciding with the period of peak CAPE. CIN remains strongly negative during nighttime hours and begins to erode from 12 LST onward, reaching its minimum around 15 LST in concert with the precipitation peak. Notably, although CAPE attains substantial values as early as 09–12 LST, precipitation is not triggered immediately because the residual CIN continues to constrain convective development. This behaviour is consistent with the DCAPE-based trigger implemented in JRA-3Q, which requires not only that CAPE exceeds a predefined threshold but also that the rate of CAPE generation by large-scale dynamical processes, such as moisture convergence and free-tropospheric lifting, is sufficiently high to active convection. By conditioning convective onset on both thermodynamic instability and large-scale dynamical forcing, the DCAPE approach effectively reproduces the observed phase lag between the surface flux maximum and the precipitation peak.

In ERA5, CAPE reaches its peak phase near 12 LST, which is approximately three hours earlier than in JRA-3Q, with precipitation increasing concurrently to peak at 12–15 LST. CIN follows a pattern similar to JRA-3Q, decreasing from 12 LST and reaching its minimum at 15 LST; however, because CAPE attains its threshold earlier, convection is initiated before CIN is fully eroded. This phase alignment between the CAPE maximum and precipitation onset indicates that the modified Tiedtke scheme (Bechtold et al., 2008, 2014) activates convection as soon as CAPE threshold is met, rapidly depleting the available instability through its CAPE-based closure on short timescales. Such tight coupling between convective triggering and boundary layer destabilization prevents the model from adequately reproducing the observed lag, as convection responds too directly to local thermodynamic instability without the necessary modulation from large-scale dynamical forcing.

MERRA-2 exhibits a different relationship between CAPE and precipitation compared to other products. CAPE reaches its maximum at 18 LST, occurring after the precipitation peak at 09–12 LST, effectively decoupling instability from precipitation. In contrast to ERA5 and JRA-3Q, CIN in MERRA-2 begins to decrease rapidly from 09 LST, indicating an earlier release of boundary layer instability. This indicates that the Relaxed Arakawa-Schubert (RAS) convective scheme with Tokioka-type trigger (Bacmeister and Stephens, 2011; Gelaro et al., 2017) fails to efficiently convert accumulated CAPE into CP, thereby permitting instability to continue building through the afternoon despite the occurrence of precipitation. Instead,

https://doi.org/10.5194/egusphere-2026-2867
Preprint. Discussion started: 3 June 2026

790 the precipitation peak aligns with the maximum phase of E between 09 and 15 LST and the strongest daytime MFC convergence among the three products, suggesting that MERRA-2 precipitation responds more directly to instantaneous moisture availability than to the cyclic evolution of thermodynamic instability. This behaviour is consistent with the LSP-dominant partitioning (cf., Fig. 8), where suppressed convective activity shifts the burden of precipitation generation toward large-scale condensation processes.

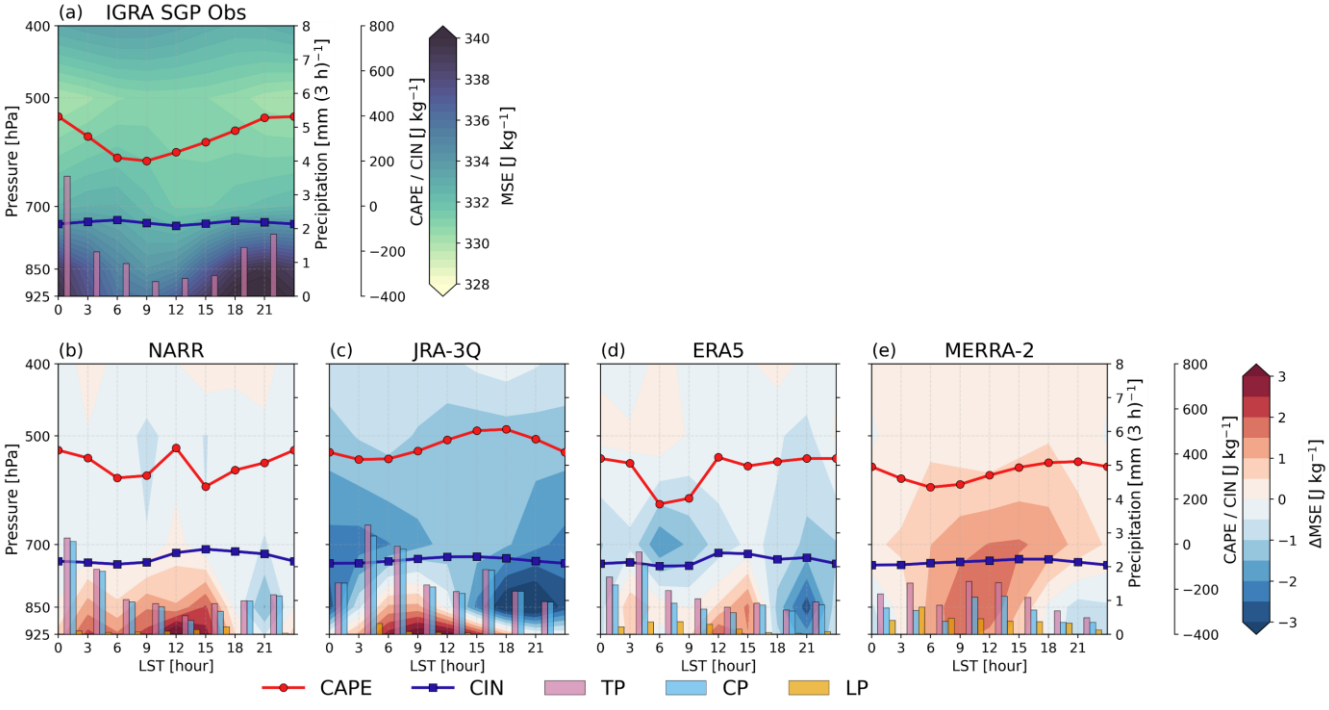

795

Figure 10: Diurnal variations of vertical profiles of moist static energy (MSE) from (a) IGRA observation, (b) NARR, (c) JRA-3Q, (d) ERA5, and (e) MERRA-2 at ARM SGP site (Lamont, Oklahoma; 36.6°N, 97.5°W), but reanalysis datasets show the bias of MSE (bottom row). In each panel, bar represents total (red), convective (blue), and large-scale (yellow) precipitation and red and blue lines indicate CAPE and CIN, respectively.

800 The preceding analysis over the NH land domain revealed that all reanalysis products exhibit premature phase lead in precipitation, driven primarily by early triggered convection (Figs. 8, 9). However, regional performance exhibits considerable variability. In the central U.S. SGP, for example, rat_{subD} exceeds 50% of the total precipitation variance in observations, whereas reanalyses capture only approximately 20%. This region also displays significant diurnal phase discrepancies between reanalyses and observations (cf. Fig. 5). Furthermore, ARM SGP site (36.6°N, 97.5°W) is characterized by a nocturnal
805 precipitation maximum that results from the complex interplay of several factors: MCSs propagating eastward from the Rocky Mountains, the Great Plains LLJ that intensifies after sunset to transport moisture from the Gulf of Mexico, and elevated convection triggered above a stable nocturnal boundary layer (Cui et al., 2021; Higgins et al., 1997; Lee et al., 2007; Shapiro

https://doi.org/10.5194/egusphere-2026-2867
Preprint. Discussion started: 3 June 2026

et al., 2016). Given its established role as a critical benchmark for evaluating model fidelity, we utilize this site to provide a detailed diagnosis of the physical processes underlying the diurnal phase biases identified in reanalysis datasets.

IGRA radiosonde observations elucidate the thermodynamic structure supporting nocturnal convection at the ARM SGP site (Fig. 10a). MSE increases throughout the lower to middle troposphere (925–700 hPa) during daytime hours (09–18 LST) as surface heating warms and moistens the boundary layer, with near-surface values exceeding 340 kJ kg^{-1}. CAPE reaches its diurnal minimum (approximately 200 J kg^{-1}) at 06 LST, then increases progressively to reach its maximum (400 J kg^{-1}) at 00 LST. Notably, although CAPE reaches substantial values during the afternoon (e.g., approximately 300 J kg^{-1} at 18 LST), precipitation remains suppressed as residual CIN continues to constrain convective initiation despite the significant thermodynamic instability. Following sunset, the intensification of the LLJ transports warm and moist air from the Gulf of Mexico, sustaining elevated MSE in the lower troposphere. Consequently, the thermodynamic constraints of the daytime are overcome by this nocturnal dynamical forcing, and convective activity at this site is predominantly confined to the nocturnal period (00–03 LST).

Reanalysis MSE biases elucidate the discrepancies in how each product represents the SGP thermodynamic structure (Fig. 10b–e). Given that MSE in the lower troposphere is predominantly governed by variations in specific humidity, these biases primarily reflect systematic errors in the moisture field. NARR exhibits positive biases at 925 hPa but negligible biases in the mid-troposphere (700–500 hPa), suggesting that the vertical moisture distribution associated with the nocturnal LLJ is most faithfully reproduced. In contrast, both JRA-3Q and ERA5 show positive biases in the lower troposphere alongside negative biases in the mid-troposphere, indicating an insufficient representation of mid-troposphere moisture transport by the LLJ. MERRA-2 presents a distinctly different pattern, with vertically pervasive positive biases, indicating a systematic overestimation of atmospheric moisture. Despite this moisture excess, MERRA-2 produces the weakest nocturnal precipitation of all products. This is consistent with the lower precipitation efficiency identified in MERRA-2 (Song and Wei, 2021), whereby suppressed ascending motion limits the conversion of atmospheric moisture into precipitation. Conversely, insufficient precipitation may allow atmospheric moisture to accumulate further, thereby reinforcing the positive humidity bias. This finding is also consistent with the LSP-dominant regime identified in Fig. 8.

https://doi.org/10.5194/egusphere-2026-2867
Preprint. Discussion started: 3 June 2026

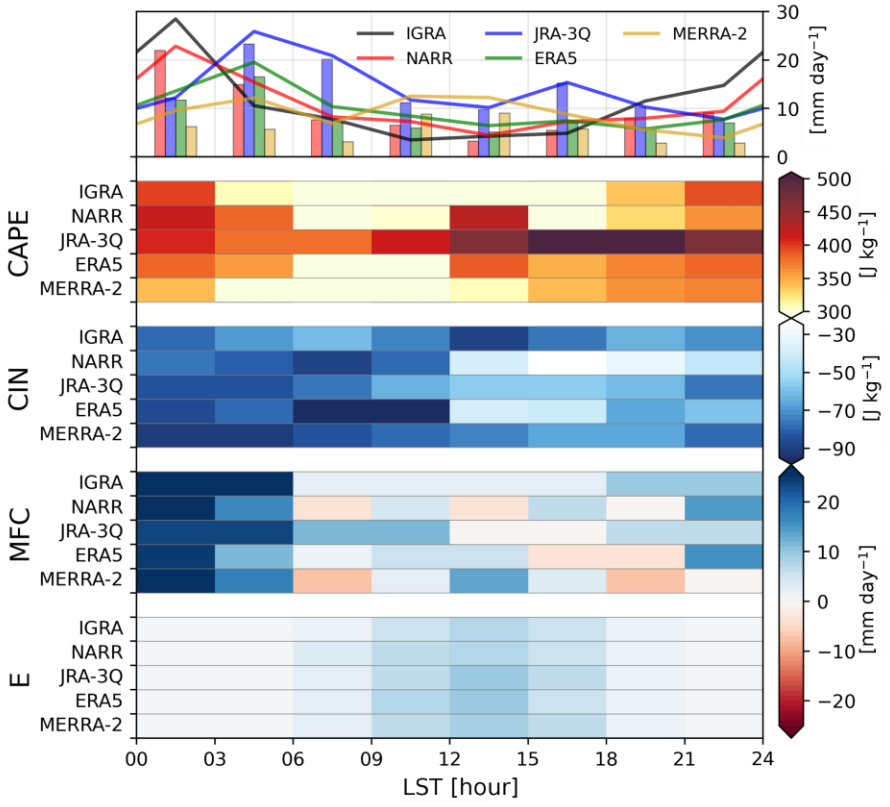

Figure 11: Same as Fig. 9, but for ARM SGP site, where results from IGRA observation and NARR reanalysis are included.

To evaluate the fidelity of reanalysis products in simulating the diurnal cycle of precipitation at the U.S. SGP site, we examine the diurnal evolution of key variables governing precipitation occurrence (Fig. 11). *E* shows similar peaks during 09–15 LST across all products at the SGP site. However, unlike the NH land average where *E* provides the essential precondition for convective development, nocturnal precipitation dominates at the SGP site and daytime *E* does not directly contribute to the nocturnal precipitation maximum (cf., Fig. 9). Observations indicate that MFC serves as the primary moisture source for nocturnal precipitation in this region, rather than daytime moisture supply from the land surface. Observed MFC begins to increase after 18 LST and reaches peak values up to 20 mm day^{-1} during 00–06 LST, coinciding with the precipitation peak. The moisture budget comparison further elucidates the differences in how each product represents this process. Furthermore, the diurnal phase relationship between CAPE and precipitation demonstrates that the product-specific characteristics identified in the NH-mean analysis are consistently manifested at the SGP site (cf., Fig. 9). In IGRA observations, CIN peaks at 12–15 LST, as the level of free convection (LFC) rises to its highest level while the lifting condensation level (LCL) remains relatively invariant across the diurnal cycle (not shown). Observed CAPE reaches its maximum at 00 LST, which is aligned with the nocturnal precipitation peak.

https://doi.org/10.5194/egusphere-2026-2867
Preprint. Discussion started: 3 June 2026

NARR successfully reproduces both the nocturnal CAPE maximum and the MFC peak phase, exhibiting the strongest nocturnal convergence among the products. This results in a precipitation peak at 00–03 LST that most closely matches the observations. In contrast, JRA-3Q and ERA5 exhibit weaker nocturnal MFC values compared to NARR. JRA-3Q shows a double-peak structure: an afternoon peak (15–18 LST) driven by the CAPE maximum as CIN erodes to its minimum (12–18 LST), and a nocturnal peak (03–06 LST) driven by MFC. However, this nocturnal precipitation phase is delayed by approximately 3 hours relative to both the observed peak and its own MFC maximum, possibly due to insufficient mid-troposphere moisture supply. ERA5 similarly displays a broad nocturnal peak between 03 and 06 LST, representing a consistent 3-hour phase delay. Despite a pronounced CAPE maximum near 12–15 LST, ERA5 does not develop significant daytime precipitation, instead responding to nocturnal MFC but with a delayed conversion. Notably, MERRA-2 presents a distinct moisture budget structure; while it captures nocturnal MFC, it also exhibits an additional strong daytime convergence peak at 12 LST and divergence at 18 LST, distinguishing its MFC diurnal evolution from the other products. MERRA-2 exhibits a relatively weak diurnal cycle in CAPE and a distinct mismatch between instability and rainfall. The persistence of instability without strong convective development indicates that accumulated energy is not efficiently released, consistent with the decoupled CAPE–precipitation relationship identified in the NH-mean analysis (Fig. 9).

Consequently, the disparate performance among reanalysis products at the SGP site is fundamentally rooted in three key factors: the representation of nocturnal MFC, the efficiency of converting accumulated instability into CP, and the fidelity of mid-troposphere moisture transport by the LLJ (Song et al., 2013; Xie and Zhang, 2000). Among the evaluated products, NARR's superior performance in capturing these processes is consistent with the constraining effect of precipitation assimilation via latent heating nudging. This technique converts observed precipitation into vertical latent heating profiles and incorporates them into the temperature tendency equation, effectively constraining the convective and grid-scale schemes to produce precipitation at observed times (Lin et al., 1999; Mesinger et al., 2006). Beyond the SGP site, NARR exhibits the smallest phase biases and the highest correlations with observations across the broader CONUS domain (cf. Fig. 7). Accordingly, for representative sites in the southeastern U.S. where direct IGRA observations are unavailable, NARR is utilized as a reliable reference to further diagnose the diurnal precipitation characteristics of the other reanalysis products.

https://doi.org/10.5194/egusphere-2026-2867
Preprint. Discussion started: 3 June 2026

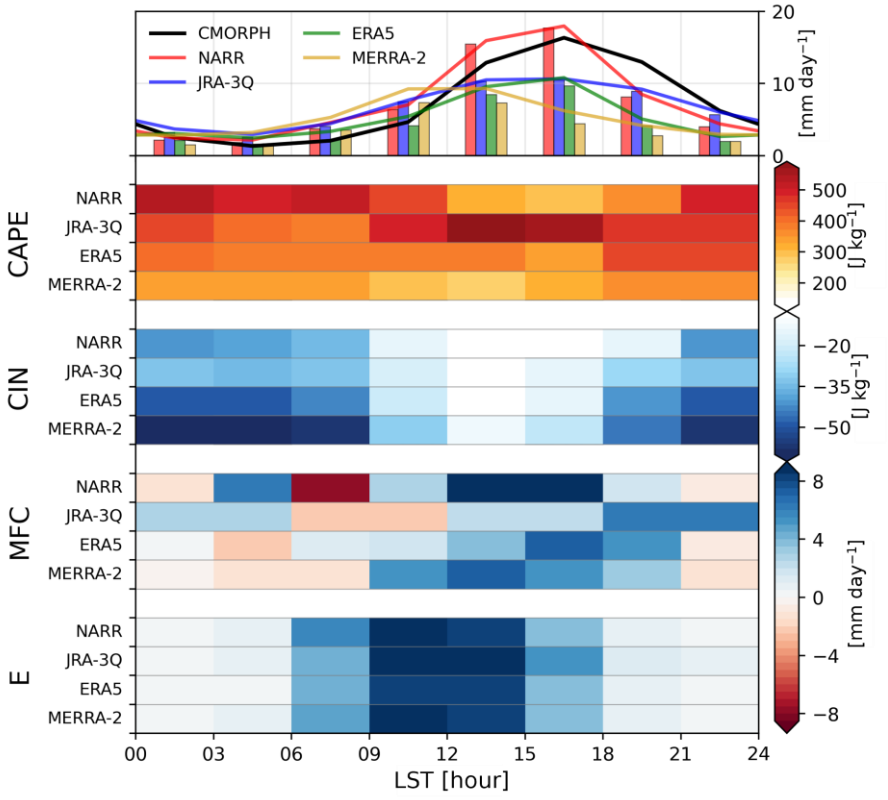

Figure 12: Same as Fig. 11, but for the southeastern point (33.5°N, 82°W).

The southeastern U.S. point (33.5°N, 82°W), located near Augusta, Georgia, presents a contrasting case to the SGP (Fig. 11). Summertime precipitation at this location is predominantly governed by the influx of abundant lower-tropospheric moisture along the western periphery of the North Atlantic Subtropical High (NASH) and intense daytime solar heating, which collectively drive CP during the afternoon (Diem, 2006; Li et al., 2012). Unlike the SGP site, convection here is initiated by daytime boundary layer thermodynamic instability (Rickenbach et al., 2015, 2020), though orographic effects from the Appalachian Mountains may also contribute as a secondary factor through eastward-propagating convective systems (Parker and Ahijevych, 2007). This site, therefore, provides a complementary framework for evaluating how reanalysis convective parameterizations respond to boundary layer thermodynamic forcing, specifically for diagnosing the roles of *E* and MFC.

CMORPH reveals a distinct precipitation maximum at 15–18 LST, characterized by land-surface thermodynamic forcing. Among the reanalysis products, NARR demonstrates the highest fidelity in reproducing both the phase and amplitude of the observed diurnal cycle. While ERA5 captures the correct peak phase, it consistently underestimates the precipitation intensity, indicating a dampened convective response to surface forcing. Conversely, JRA-3Q exhibits a 3-hour phase lead with a peak at 12–15 LST, and MERRA-2 displays a notably weak, plateau-like distribution spanning 09 to 15 LST.

https://doi.org/10.5194/egusphere-2026-2867
Preprint. Discussion started: 3 June 2026

The timing and intensity of convection are regulated by the diurnal evolution of boundary layer instability and inhibition. In NARR and ERA5, CAPE reaches a nocturnal maximum and an afternoon minimum, establishing an anti-phase relationship with precipitation. This nocturnal accumulation is sustained by the preservation of boundary layer moisture from daytime evaporation and free-tropospheric radiative cooling. Convective initiation occurs only after surface heating erodes the CIN to a near-zero minimum between 12 and 18 LST, facilitating the rapid release of stored energy. In contrast, JRA-3Q utilizes a DCAPE-based triggering mechanism that activates convection prematurely while CAPE is still being generated by surface heating, resulting in a coupled CAPE-precipitation relationship and reduced convective intensity. MERRA-2, characterized by the largest nocturnal CIN, undergoes an abrupt reduction in inhibition at 09 LST, which triggers a premature and temporally dispersed release of instability, thereby explaining its plateau-like precipitation structure.

The moisture budget at this site further highlights the distinction between thermodynamic preconditioning and dynamical feedback. Across all evaluated products, *E* peaks between 09 and 15 LST, serving as a critical preconditioning process that moistens the boundary layer and reduces the gap between the LCL and the LFC. While *E* establishes the necessary thermodynamic environment, MFC reveals the dynamic response to convective development. In NARR, the MFC peak during 12–18 LST signifies that convection-induced mesoscale convergence acts as a positive feedback to amplify thermodynamically initiated precipitation. This feedback-driven intensification is followed by an abrupt decline in precipitation at 18–21 LST, contrasting with the more symmetrical development and decay observed in CMORPH. ERA5 exhibits a qualitatively similar structure, but its consistent underestimation of the afternoon precipitation amplitude is primarily tied to a weaker MFC response. Furthermore, the rapid decay of precipitation in ERA5 after 18 LST is driven by its relatively high CIN, which reflects a faster post-convective stabilization of the lower troposphere compared to other products. On the other hand, JRA-3Q displays prolonged MFC even after the cessation of *E* during 18–24 LST. This sustained moisture convergence, combined with its notably weak CIN, facilitates a gradual rather than sharp decay in precipitation throughout the late evening hours.

5 Summary and Conclusions

This study provides a comprehensive evaluation of sub-daily precipitation variability and diurnal cycle characteristics across five satellite-based products (IMERG, TRMM, CMORPH, GSMaP, and MSWEP) and four reanalysis datasets (ERA5, JRA-3Q, MERRA-2, and NARR), benchmarked against 6,824 ground-based observations over the Northern Hemisphere during boreal summer. By simultaneously quantifying sub-daily variance fractions, decomposing harmonic structures, and diagnosing the physical mechanisms underlying diurnal phase shifts through atmospheric moisture budget analysis complemented by radiosonde observations, this study advances beyond previous intercomparisons confined to satellite products or limited observation sites.

Ground-based observations establish that sub-daily fluctuations account for 66.3% of total precipitation variance, with the irregular component reflecting convective intermittency and episodic MCS occurrence dominating (approximately 98%) over

https://doi.org/10.5194/egusphere-2026-2867
Preprint. Discussion started: 3 June 2026

the repeatable diurnal signal. All evaluated datasets underestimate this fraction, most severely in reanalysis products, where coarse-resolution parameterization schemes suppress intense sub-daily events while producing excessively frequent light rainfall. This finding underscores that current datasets struggle not only with the timing of the diurnal cycle but with the fundamental partitioning of precipitation energy across sub-daily time scales. Harmonic decomposition of the regular component further reveals that while the first harmonic (24-hour period) dominates across all products, reanalysis datasets exhibit a spurious amplification of the semi-diurnal component. Notably, the apparent agreement of the multi-model mean with the observed first harmonic fraction is a statistical artifact of mutual cancellation between ERA5's semi-diurnal excess and JRA-3Q's first harmonic overestimation, rather than a physically consistent reproduction of the observed spectral balance.

Satellite products reproduce the observed afternoon precipitation peak (approximately 17 LST) with a systematic 1–2 hour delay, attributable to passive microwave sensors detecting upper-tropospheric ice-scattering signals rather than surface precipitation. Among satellite products, CMORPH demonstrates superior performance in reproducing both the observed diurnal phase and the absolute magnitude of the 1st harmonic amplitude (σ_{1st}^2). This outcome reflects a clear design principle: a retrieval framework that preserves the physical timing of precipitation signals through morphing-based propagation of PMW observations, paired with a bias correction approach with PDF matching that achieves climatological accuracy without directly constraining hourly magnitudes and thus maintains the integrity of sub-daily temporal structures. In contrast, products that directly adjust hourly magnitudes to match daily gauge totals risk suppressing the diurnal signals they aim to represent, as evidenced by GSMaP's reversed land–ocean contrast in sub-daily variance. MSWEP similarly inherits an early phase bias from its use of ERA5 for sub-daily temporal disaggregation, illustrating that the choice of reanalysis input can fundamentally compromise the diurnal fidelity of merged satellite products. Regional evaluation reveals that satellite products achieve the strongest phase correlations over the CONUS ($r > 0.8$), with moderate agreement over East Asia and the weakest performance over Europe, where complex topography and diverse precipitation regimes increase spatial variability.

Reanalysis products exhibit a more severe and physically distinct premature phase lead over land, increasing from JRA-3Q (16 LST) to ERA5 (14 LST) to MERRA-2 (12 LST), driven exclusively by premature convective triggering rather than large-scale precipitation processes. In addition to the phase bias, all reanalysis products systematically underestimate the absolute magnitude of σ_{1st}^2, indicating that their deficiencies extend beyond timing errors to encompass an insufficient physical intensity of the diurnal cycle itself. Among them, JRA-3Q demonstrates the smallest phase bias and the closest amplitude to observations. This relative success is consistent with the design rationale of its DCAPE-based trigger, which conditions convective onset on both CAPE threshold and the rate of CAPE generation by large-scale dynamical forcing. This additional constraint naturally reproduces the observed lag between surface heating and precipitation onset, and its relative success highlights that the design of convective trigger functions is the single most important determinant of diurnal cycle fidelity in reanalysis products. The consistency of evapotranspiration forcing across all reanalysis products further confirms that surface moisture supply is not the primary source of inter-product phase differences; rather, structural differences in how each convective parameterization responds to boundary layer destabilization govern the divergence in precipitation timing.

https://doi.org/10.5194/egusphere-2026-2867
Preprint. Discussion started: 3 June 2026

These parameterization-driven biases are consistently manifested across contrasting precipitation regimes. Diagnosis at the ARM SGP site characterized by nocturnal MCS-driven precipitation, and at the southeastern U.S. site governed by daytime thermodynamic forcing, confirms that phase errors are structural limitations of convective parameterization rather than region-specific artifacts. At the SGP site, NARR uniquely reproduces the observed nocturnal precipitation maximum through direct assimilation of precipitation observations via latent heating nudging, demonstrating that precipitation data assimilation can effectively constrain convective timing even where model physics alone fails. Together, the contrasting performances of JRA-3Q and NARR point to two complementary pathways for improving reanalysis diurnal cycle representation: advancing the physical realism of convective trigger functions to incorporate large-scale dynamical constraints and expanding the direct assimilation of sub-daily precipitation observations.

The findings of this study have broad implications across multiple disciplines that rely on accurate sub-daily precipitation information. Errors in diurnal precipitation timing and intensity in reanalysis products can propagate into the representation of land-atmosphere energy and moisture exchanges, bias hydrological simulations of streamflow, and compromise the evaluation of convective parameterization schemes in climate models. The accurate representation of the diurnal cycle is therefore not a narrow modelling concern but a cross-cutting requirement for advances in weather forecasting, climate projection, and water resource management. Critically, the severe underestimation of irregular sub-daily variance identified here is not confined to a single product class but is pervasive across both satellite and reanalysis datasets, pointing to a fundamental gap in the representation of precipitation intermittency that transcends differences in retrieval methodology or data assimilation strategy.

This study is necessarily limited to Northern Hemisphere land regions during boreal summer, where long-term sub-daily gauge records are sufficiently dense to support robust evaluation. Extending the analysis to the Southern Hemisphere, tropical regions, and additional seasons, where diurnal forcing mechanisms and dominant precipitation regimes differ substantially from those examined here, remains an important priority for future work. The evaluation of convection-permitting reanalyses, which explicitly resolve mesoscale convective dynamics rather than relying on parameterization, offers a particularly promising avenue for determining whether higher-fidelity process representation can systematically reduce the biases identified here. Additionally, the rapid emergence of AI-based forecast models such as ECMWF's Artificial Intelligence Forecasting System (AIFS; Lang et al., 2024) raises new questions about whether data-driven approaches inherit the phase shift of their training data or reproduce observed diurnal precipitation characteristics more faithfully, which warrants future investigation. The diagnostic framework presented in this study, which integrates sub-daily variance decomposition, harmonic analysis, and atmospheric moisture budget diagnosis benchmarked against an extensive ground-based observational network, provides a transferable methodology for such future assessments and offers a rigorous basis for the selection and development of sub-daily precipitation products in hydrological and climate research.

https://doi.org/10.5194/egusphere-2026-2867
Preprint. Discussion started: 3 June 2026

Code availability

The analysis code used in this study is available on GitHub (https://github.com/Gyu-kite/Diurnal-cycle-choi-2026, last access: 18 May 2026) and archived on Zenodo (https://doi.org/10.5281/zenodo.19563213) (Choi, 2026).

Data availability

Ground-based observations used in this study are available from the following sources. A subset of the Global Sub-Daily Rainfall dataset (GSDR; Lewis et al., 2019) is available from Zenodo (https://doi.org/10.5281/zenodo.8369987). HadISD station data are available from the UK Met Office Hadley Centre (https://www.metoffice.gov.uk/hadobs/hadisd/, last access: 18 May 2026). German Weather Service (DWD) station observations are available from the DWD Climate Data Center (https://cdc.dwd.de/, last access: 18 May 2026). Environment and Climate Change Canada (ECCC) station data are available from the ECCC climate data portal (https://climate.weather.gc.ca/, last access: 18 May 2026). Korea Meteorological Administration (KMA) station data are available from the KMA Open MET Data Portal (https://data.kma.go.kr, last access: 18 May 2026), subject to the provider's data policy and registration. The China Meteorological Forcing Dataset (CMFD; He et al., 2020) is available from the National Tibetan Plateau Data Center/CASEarth portal (https://data.casearth.cn/thematic/CS/647, last access: 18 May 2026).

Satellite precipitation products are available from the following sources. GPM IMERG and TRMM precipitation products are available from the NASA Goddard Earth Sciences Data and Information Services Center (GES DISC; https://disc.gsfc.nasa.gov/, last access: 18 May 2026). CMORPH satellite precipitation data are available from the NOAA National Centers for Environmental Information (https://www.ncei.noaa.gov/products/climate-data-records/precipitation-cmorph, last access: 18 May 2026). GSMaP precipitation products are available from the JAXA Earth Observation Research Center via the GSMaP data portal (registration required; https://sharaku.eorc.jaxa.jp/GSMaP/, last access: 18 May 2026). MSWEP precipitation data are available for non-commercial research use from GloH2O (https://www.gloh2o.org/mswep/, last access: 18 May 2026).

Reanalysis datasets are available from the following sources. ERA5 reanalysis data are available from the Copernicus Climate Data Store (https://cds.climate.copernicus.eu/, last access: 18 May 2026). JRA-3Q reanalysis data are available from the Japan Meteorological Agency (https://www.data.jma.go.jp/jra/html/JRA-3Q/index_en.html, last access: 18 May 2026) and through the DIAS/JRA-3Q collection on Zenodo (https://zenodo.org/communities/tpchange, last access: 18 May 2026). MERRA-2 reanalysis data are available from the NASA GES DISC (https://disc.gsfc.nasa.gov/, last access: 18 May 2026). The North American Regional Reanalysis (NARR) is available from the NCAR Research Data Archive (https://rda.ucar.edu/datasets/ds608.0/, last access: 18 May 2026).

https://doi.org/10.5194/egusphere-2026-2867
Preprint. Discussion started: 3 June 2026

Author contributions

Conceptualization: GC and ES. Investigation, methodology, and formal analysis: GC, ES, and PAD. Writing (original draft preparation): GC. Writing (review and editing): ES and PAD.

Competing interests

The contact author has declared that none of the authors has any competing interests.

Acknowledgements

This research was supported by the National Research Foundation of Korea (NRF) grant funded by the Korea government (MSIT) (RS-2026-25479797). Gyuyeon Choi was supported by the Korea Meteorological Administration Research and Development Program under Grant (RS-2025-02313090).

Financial support

This research has been supported by the National Research Foundation of Korea (NRF) under RS-2025-02363044 and the Korea Meteorological Administration Research and Development Program under RS-2025-02313090.

https://doi.org/10.5194/egusphere-2026-2867
Preprint. Discussion started: 3 June 2026

References

Adler, R., Sapiano, M., Huffman, G., Wang, J.-J., Gu, G., Bolvin, D., Chiu, L., Schneider, U., Becker, A., Nelkin, E., Xie, P., Ferraro, R., and Shin, D.-B.: The Global Precipitation Climatology Project (GPCP) Monthly Analysis (New Version 2.3) and a Review of 2017 Global Precipitation, Atmosphere, 9, 138, https://doi.org/10.3390/atmos9040138, 2018.

Afonso, J. M. de S., Vila, D. A., Gan, M. A., Quispe, D. P., Barreto, N. de J. da C., Huamán Chinchay, J. H., and Palharini, R. S. A.: Precipitation Diurnal Cycle Assessment of Satellite-Based Estimates over Brazil, Remote Sens., 12, 2339, https://doi.org/10.3390/rs12142339, 2020.

Ahn, M.-S., Gleckler, P. J., Lee, J., Pendergrass, A. G., and Jakob, C.: Benchmarking Simulated Precipitation Variability Amplitude across Time Scales, J. Clim., 35, 3173–3196, https://doi.org/10.1175/JCLI-D-21-0542.1, 2022.

Allan, R. P., Barlow, M., Byrne, M. P., Cherchi, A., Douville, H., Fowler, H. J., Gan, T. Y., Pendergrass, A. G., Rosenfeld, D., Swann, A. L. S., Wilcox, L. J., and Zolina, O.: Advances in understanding large-scale responses of the water cycle to climate change, Ann. N. Y. Acad. Sci., 1472, 49–75, https://doi.org/10.1111/nyas.14337, 2020.

Bacmeister, J. T. and Stephens, G. L.: Spatial statistics of likely convective clouds in CloudSat data, J. Geophys. Res. Atmospheres, 116, https://doi.org/10.1029/2010JD014444, 2011.

Balsamo, G., Beljaars, A., Scipal, K., Viterbo, P., Van Den Hurk, B., Hirschi, M., and Betts, A. K.: A Revised Hydrology for the ECMWF Model: Verification from Field Site to Terrestrial Water Storage and Impact in the Integrated Forecast System, J. Hydrometeorol., 10, 623–643, https://doi.org/10.1175/2008JHM1068.1, 2009.

Bechtold, P., Köhler, M., Jung, T., Doblas-Reyes, F., Leutbecher, M., Rodwell, M. J., Vitart, F., and Balsamo, G.: Advances in simulating atmospheric variability with the ECMWF model: From synoptic to decadal time-scales, Q. J. R. Meteorol. Soc., 134, 1337–1351, https://doi.org/10.1002/qj.289, 2008.

Bechtold, P., Semane, N., Lopez, P., Chaboureau, J.-P., Beljaars, A., and Bormann, N.: Representing Equilibrium and Nonequilibrium Convection in Large-Scale Models, J. Atmospheric Sci., 71, 734–753, https://doi.org/10.1175/JAS-D-13-0163.1, 2014.

Beck, H. E., Wood, E. F., Pan, M., Fisher, C. K., Miralles, D. G., Van Dijk, A. I. J. M., McVicar, T. R., and Adler, R. F.: MSWEP V2 Global 3-Hourly 0.1° Precipitation: Methodology and Quantitative Assessment, Bull. Am. Meteorol. Soc., 100, 473–500, https://doi.org/10.1175/BAMS-D-17-0138.1, 2019.

Bloom, S. C., Takacs, L. L., Da Silva, A. M., and Ledvina, D.: Data Assimilation Using Incremental Analysis Updates, Mon. Weather Rev., 124, 1256–1271, https://doi.org/10.1175/1520-0493(1996)124%3C1256:DAUIAU%3E2.0.CO;2, 1996.

Catto, J. L., Jakob, C., Berry, G., and Nicholls, N.: Relating global precipitation to atmospheric fronts, Geophys. Res. Lett., 39, https://doi.org/10.1029/2012GL051736, 2012.

Chen, H., Yong, B., Gourley, J. J., Liu, J., Ren, L., Wang, W., Hong, Y., and Zhang, J.: Impact of the crucial geographic and climatic factors on the input source errors of GPM-based global satellite precipitation estimates, J. Hydrol., 575, 1–16, https://doi.org/10.1016/j.jhydrol.2019.05.020, 2019.

https://doi.org/10.5194/egusphere-2026-2867
Preprint. Discussion started: 3 June 2026

Chen, M., Dickinson, R. E., Zeng, X., and Hahmann, A. N.: Comparison of Precipitation Observed over the Continental United States to That Simulated by a Climate Model, J. Clim., 9, 2233–2249, https://doi.org/10.1175/1520-0442(1996)009%3C2233:COPOOT%3E2.0.CO;2, 1996.

Christopoulos, C. and Schneider, T.: Assessing Biases and Climate Implications of the Diurnal Precipitation Cycle in Climate Models, Geophys. Res. Lett., 48, e2021GL093017, https://doi.org/10.1029/2021GL093017, 2021.

Covey, C., Gleckler, P. J., Doutriaux, C., Williams, D. N., Dai, A., Fasullo, J., Trenberth, K., and Berg, A.: Metrics for the Diurnal Cycle of Precipitation: Toward Routine Benchmarks for Climate Models, J. Clim., 29, 4461–4471, https://doi.org/10.1175/JCLI-D-15-0664.1, 2016.

Covey, C., Doutriaux, C., Gleckler, P. J., Taylor, K. E., Trenberth, K. E., and Zhang, Y.: High-Frequency Intermittency in Observed and Model-Simulated Precipitation, Geophys. Res. Lett., 45, 12,514-12,522, https://doi.org/10.1029/2018GL078926, 2018.

Cui, Z., Zhang, G. J., Wang, Y., and Xie, S.: Understanding the Roles of Convective Trigger Functions in the Diurnal Cycle of Precipitation in the NCAR CAM5, J. Clim., 34, 6473–6489, https://doi.org/10.1175/JCLI-D-20-0699.1, 2021.

Dai, A.: Global Precipitation and Thunderstorm Frequencies. Part II: Diurnal Variations, J. Clim., 14, 1112–1128, https://doi.org/10.1175/1520-0442(2001)014%3C1112:GPATFP%3E2.0.CO;2, 2001.

Dai, A.: Precipitation Characteristics in Eighteen Coupled Climate Models, J. Clim., 19, 4605–4630, https://doi.org/10.1175/JCLI3884.1, 2006b.

Dai, A.: The diurnal cycle from observations and ERA5 in precipitation, clouds, boundary layer height, buoyancy, and surface fluxes, Clim. Dyn., 62, 5879–5908, https://doi.org/10.1007/s00382-024-07182-6, 2024.

Dai, A. and Trenberth, K. E.: The Diurnal Cycle and Its Depiction in the Community Climate System Model, J. Clim., 17, 930–951, https://doi.org/10.1175/1520-0442(2004)017%3C0930:TDCAID%3E2.0.CO;2, 2004.

Dai, A., Giorgi, F., and Trenberth, K. E.: Observed and model-simulated diurnal cycles of precipitation over the contiguous United States, J. Geophys. Res. Atmospheres, 104, 6377–6402, https://doi.org/10.1029/98JD02720, 1999.

Dai, A., Lin, X., and Hsu, K.-L.: The frequency, intensity, and diurnal cycle of precipitation in surface and satellite observations over low- and mid-latitudes, Clim. Dyn., 29, 727–744, https://doi.org/10.1007/s00382-007-0260-y, 2007.

Dai, A., Qian, T., Trenberth, K. E., and Milliman, J. D.: Changes in Continental Freshwater Discharge from 1948 to 2004, J. Clim., 22, 2773–2792, https://doi.org/10.1175/2008JCLI2592.1, 2009.

Daly, C., Neilson, R. P., and Phillips, D. L.: A Statistical-Topographic Model for Mapping Climatological Precipitation over Mountainous Terrain, J. Appl. Meteorol., 33, 140–158, https://doi.org/10.1175/1520-0450(1994)033%3C0140:ASTMFM%3E2.0.CO;2, 1994.

Deser, C. and Smith, C. A.: Diurnal and Semidiurnal Variations of the Surface Wind Field over the Tropical Pacific Ocean, J. Clim., 11, 1730–1748, https://doi.org/10.1175/1520-0442(1998)011%3C1730:DASVOT%3E2.0.CO;2, 1998b.

Diem, J. E.: Synoptic-Scale Controls of Summer Precipitation in the Southeastern United States, https://doi.org/10.1175/JCLI3645.1, 2006.

https://doi.org/10.5194/egusphere-2026-2867
Preprint. Discussion started: 3 June 2026

Dirmeyer, P. A., Cash, B. A., Kinter, J. L., Jung, T., Marx, L., Satoh, M., Stan, C., Tomita, H., Towers, P., Wedi, N., Achuthavarier, D., Adams, J. M., Altshuler, E. L., Huang, B., Jin, E. K., and Manganello, J.: Simulating the diurnal cycle of rainfall in global climate models: resolution versus parameterization, Clim. Dyn., 39, 399–418, https://doi.org/10.1007/s00382-011-1127-9, 2012.

Dirmeyer, P. A., Chen, L., Wu, J., Shin, C.-S., Huang, B., Cash, B. A., Bosilovich, M. G., Mahanama, S., Koster, R. D., Santanello, J. A., Ek, M. B., Balsamo, G., Dutra, E., and Lawrence, D. M.: Verification of Land–Atmosphere Coupling in Forecast Models, Reanalyses, and Land Surface Models Using Flux Site Observations, https://doi.org/10.1175/JHM-D-17-0152.1, 2018.

Donat, M. G., Alexander, L. V., Yang, H., Durre, I., Vose, R., Dunn, R. J. H., Willett, K. M., Aguilar, E., Brunet, M., Caesar, J., Hewitson, B., Jack, C., Klein Tank, A. M. G., Kruger, A. C., Marengo, J., Peterson, T. C., Renom, M., Oria Rojas, C., Rusticucci, M., Salinger, J., Elrayah, A. S., Sekele, S. S., Srivastava, A. K., Trewin, B., Villarroel, C., Vincent, L. A., Zhai, P., Zhang, X., and Kitching, S.: Updated analyses of temperature and precipitation extreme indices since the beginning of the twentieth century: The HadEX2 dataset, J. Geophys. Res. Atmospheres, 118, 2098–2118, https://doi.org/10.1002/jgrd.50150, 2013.

Dong, W., Krasting, J. P., and Guo, H.: Analysis of Precipitation Diurnal Cycle and Variance in Multiple Observations, CMIP6 Models, and a Series of GFDL-AM4.0 Simulations, J. Clim., 36, 8637–8655, https://doi.org/10.1175/JCLI-D-23-0268.1, 2023.

Dunn, R. J. H., Willett, K. M., Parker, D. E., and Mitchell, L.: Expanding HadISD: quality-controlled, sub-daily station data from 1931, Geosci. Instrum. Methods Data Syst., 5, 473–491, https://doi.org/10.5194/gi-5-473-2016, 2016.

Durre, I., Vose, R. S., and Wuertz, D. B.: Overview of the Integrated Global Radiosonde Archive, https://doi.org/10.1175/JCLI3594.1, 2006.

Durre, I., Yin, X., Vose, R. S., Applequist, S., Arnfield, J., Korzeniewski, B., and Hundermark, B.: Integrated Global Radiosonde Archive (IGRA), Version 2, https://doi.org/10.7289/V5X63K0Q, 2016.

Ebert, E. E., Janowiak, J. E., and Kidd, C.: Comparison of Near-Real-Time Precipitation Estimates from Satellite Observations and Numerical Models, Bull. Am. Meteorol. Soc., 88, 47–64, https://doi.org/10.1175/BAMS-88-1-47, 2007.

Fisher, N. I. and Lee, A. J.: Time Series Analysis of Circular Data, J. R. Stat. Soc. Ser. B Methodol., 56, 327–339, 1994.

Freitas, S. R., Grell, G. A., and Li, H.: The Grell–Freitas (GF) convection parameterization: recent developments, extensions, and applications, Geosci. Model Dev., 14, 5393–5411, https://doi.org/10.5194/gmd-14-5393-2021, 2021.

Gao, R., Li, L., Wang, Y., Li, W., Yun, Z., and Gai, Y.: Improvements and limitations of the latest version 8 of GSMaP compared with its former version 7 and IMERG V06 at multiple spatio-temporal scales in mainland China, Atmospheric Res., 308, 107517, https://doi.org/10.1016/j.atmosres.2024.107517, 2024.

Gelaro, R., McCarty, W., Suárez, M. J., Todling, R., Molod, A., Takacs, L., Randles, C. A., Darmenov, A., Bosilovich, M. G., Reichle, R., Wargan, K., Coy, L., Cullather, R., Draper, C., Akella, S., Buchard, V., Conaty, A., Da Silva, A. M., Gu, W., Kim, G.-K., Koster, R., Lucchesi, R., Merkova, D., Nielsen, J. E., Partyka, G., Pawson, S., Putman, W., Rienecker, M., Schubert, S.

https://doi.org/10.5194/egusphere-2026-2867
Preprint. Discussion started: 3 June 2026

D., Sienkiewicz, M., and Zhao, B.: The Modern-Era Retrospective Analysis for Research and Applications, Version 2 (MERRA-2), J. Clim., 30, 5419–5454, https://doi.org/10.1175/JCLI-D-16-0758.1, 2017.

Gervais, M., Tremblay, L. B., Gyakum, J. R., and Atallah, E.: Representing Extremes in a Daily Gridded Precipitation Analysis over the United States: Impacts of Station Density, Resolution, and Gridding Methods, J. Clim., 27, 5201–5218, https://doi.org/10.1175/JCLI-D-13-00319.1, 2014.

Gibson, P. B., Waliser, D. E., Lee, H., Tian, B., and Massoud, E.: Climate Model Evaluation in the Presence of Observational Uncertainty: Precipitation Indices over the Contiguous United States, J. Hydrometeorol., 20, 1339–1357, https://doi.org/10.1175/JHM-D-18-0230.1, 2019.

Gray, W. M. and Jacobson, R. W.: Diurnal Variation of Deep Cumulus Convection, Mon. Weather Rev., 105, 1171–1188, https://doi.org/10.1175/1520-0493(1977)105%3C1171:DVODCC%3E2.0.CO;2, 1977.

Guilloteau, C., Foufoula-Georgiou, E., Kummerow, C. D., and Petković, V.: Resolving Surface Rain from GMI High-Frequency Channels: Limits Imposed by the Three-Dimensional Structure of Precipitation, J. Atmospheric Ocean. Technol., 35, 1835–1847, https://doi.org/10.1175/JTECH-D-18-0011.1, 2018.

Gyuyeon Choi: Gyu-kite/Diurnal-cycle-choi-2026: v1.0.2 - Diurnal cycle analysis code, , https://doi.org/10.5281/ZENODO.19563213, 2026.

Hawcroft, M. K., Shaffrey, L. C., Hodges, K. I., and Dacre, H. F.: How much Northern Hemisphere precipitation is associated with extratropical cyclones?, Geophys. Res. Lett., 39, https://doi.org/10.1029/2012GL053866, 2012.

Hayden, L. and Liu, C.: Differences in the Diurnal Variation of Precipitation Estimated by Spaceborne Radar, Passive Microwave Radiometer, and IMERG, J. Geophys. Res. Atmospheres, 126, e2020JD033020, https://doi.org/10.1029/2020JD033020, 2021.

He, C. and Li, T.: Does global warming amplify interannual climate variability?, Clim. Dyn., 52, 2667–2684, https://doi.org/10.1007/s00382-018-4286-0, 2019.

He, J., Yang, K., Tang, W., Lu, H., Qin, J., Chen, Y., and Li, X.: The first high-resolution meteorological forcing dataset for land process studies over China, Sci. Data, 7, 25, https://doi.org/10.1038/s41597-020-0369-y, 2020.

Herold, N., Alexander, L. V., Donat, M. G., Contractor, S., and Becker, A.: How much does it rain over land?, Geophys. Res. Lett., 43, 341–348, https://doi.org/10.1002/2015GL066615, 2016.

Hersbach, H., Bell, B., Berrisford, P., Hirahara, S., Horányi, A., Muñoz-Sabater, J., Nicolas, J., Peubey, C., Radu, R., Schepers, D., Simmons, A., Soci, C., Abdalla, S., Abellan, X., Balsamo, G., Bechtold, P., Biavati, G., Bidlot, J., Bonavita, M., De Chiara, G., Dahlgren, P., Dee, D., Diamantakis, M., Dragani, R., Flemming, J., Forbes, R., Fuentes, M., Geer, A., Haimberger, L., Healy, S., Hogan, R. J., Hólm, E., Janisková, M., Keeley, S., Laloyaux, P., Lopez, P., Lupu, C., Radnoti, G., De Rosnay, P., Rozum, I., Vamborg, F., Villaume, S., and Thépaut, J.: The ERA5 global reanalysis, Q. J. R. Meteorol. Soc., 146, 1999–2049, https://doi.org/10.1002/qj.3803, 2020.

https://doi.org/10.5194/egusphere-2026-2867
Preprint. Discussion started: 3 June 2026

Higgins, R. W., Yao, Y., Yarosh, E. S., Janowiak, J. E., and Mo, K. C.: Influence of the Great Plains Low-Level Jet on Summertime Precipitation and Moisture Transport over the Central United States, J. Clim., 10, 481–507, https://doi.org/10.1175/1520-0442(1997)010%3C0481:IOTGPL%3E2.0.CO;2, 1997.

Huang, P. and Xie, S.-P.: Mechanisms of change in ENSO-induced tropical Pacific rainfall variability in a warming climate, Nat. Geosci., 8, 922–926, https://doi.org/10.1038/ngeo2571, 2015.

Huffman, G. J., Bolvin, D. T., Nelkin, E. J., Wolff, D. B., Adler, R. F., Gu, G., Hong, Y., Bowman, K. P., and Stocker, E. F.: The TRMM Multisatellite Precipitation Analysis (TMPA): Quasi-Global, Multiyear, Combined-Sensor Precipitation Estimates at Fine Scales, https://doi.org/10.1175/JHM560.1, 2007.

Huffman, G. J., Bolvin, D. T., Braithwaite, D., Hsu, K.-L., Joyce, R. J., Kidd, C., Nelkin, E. J., Sorooshian, S., Stocker, E. F., Tan, J., Wolff, D. B., and Xie, P.: Integrated Multi-satellite Retrievals for the Global Precipitation Measurement (GPM) Mission (IMERG), in: Satellite Precipitation Measurement: Volume 1, edited by: Levizzani, V., Kidd, C., Kirschbaum, D. B., Kummerow, C. D., Nakamura, K., and Turk, F. J., Springer International Publishing, Cham, 343–353, https://doi.org/10.1007/978-3-030-24568-9_19, 2020.

Huffman, G. J., Adler, R. F., Behrangi, A., Bolvin, D. T., Nelkin, E. J., Gu, G., and Ehsani, M. R.: The New Version 3.2 Global Precipitation Climatology Project (GPCP) Monthly and Daily Precipitation Products, J. Clim., 36, 7635–7655, https://doi.org/10.1175/JCLI-D-23-0123.1, 2023.

Janowiak, J. E., Kousky, V. E., and Joyce, R. J.: Diurnal cycle of precipitation determined from the CMORPH high spatial and temporal resolution global precipitation analyses, J. Geophys. Res. Atmospheres, 110, https://doi.org/10.1029/2005JD006156, 2005.

Jiang, X., Adames, Á. F., Kim, D., Maloney, E. D., Lin, H., Kim, H., Zhang, C., DeMott, C. A., and Klingaman, N. P.: Fifty Years of Research on the Madden-Julian Oscillation: Recent Progress, Challenges, and Perspectives, J. Geophys. Res. Atmospheres, 125, e2019JD030911, https://doi.org/10.1029/2019JD030911, 2020.

Joyce, R. J. and Xie, P.: Kalman Filter–Based CMORPH, J. Hydrometeorol., 12, 1547–1563, https://doi.org/10.1175/JHM-D-11-022.1, 2011.

Joyce, R. J., Janowiak, J. E., Arkin, P. A., and Xie, P.: CMORPH: A Method that Produces Global Precipitation Estimates from Passive Microwave and Infrared Data at High Spatial and Temporal Resolution, J. Hydrometeorol., 5, 487–503, https://doi.org/10.1175/1525-7541(2004)005%3C0487:CAMTPG%3E2.0.CO;2, 2004.

Karger, D. N., Conrad, O., Böhner, J., Kawohl, T., Kreft, H., Soria-Auza, R. W., Zimmermann, N. E., Linder, H. P., and Kessler, M.: Climatologies at high resolution for the earth's land surface areas, Sci. Data, 4, 170122, https://doi.org/10.1038/sdata.2017.122, 2017.

Kobayashi, S., Ota, Y., Harada, Y., Ebita, A., Moriya, M., Onoda, H., Onogi, K., Kamahori, H., Kobayashi, C., Endo, H., Miyaoka, K., and Takahashi, K.: The JRA-55 Reanalysis: General Specifications and Basic Characteristics, J. Meteorol. Soc. Jpn. Ser II, 93, 5–48, https://doi.org/10.2151/jmsj.2015-001, 2015.

https://doi.org/10.5194/egusphere-2026-2867
Preprint. Discussion started: 3 June 2026

Kosaka, Y., Kobayashi, S., Harada, Y., Kobayashi, C., Naoe, H., Yoshimoto, K., Harada, M., Goto, N., Chiba, J., Miyaoka, K., Sekiguchi, R., Deushi, M., Kamahori, H., Nakaegawa, T., Tanaka, T. Y., Tokuhiro, T., Sato, Y., Matsushita, Y., and Onogi, K.: The JRA-3Q Reanalysis, J. Meteorol. Soc. Jpn. Ser II, 102, 49–109, https://doi.org/10.2151/jmsj.2024-004, 2024.

Kubota, T., Aonashi, K., Ushio, T., Shige, S., Takayabu, Y. N., Kachi, M., Arai, Y., Tashima, T., Masaki, T., Kawamoto, N., Mega, T., Yamamoto, M. K., Hamada, A., Yamaji, M., Liu, G., and Oki, R.: Global Satellite Mapping of Precipitation (GSMaP) Products in the GPM Era, in: Satellite Precipitation Measurement: Volume 1, edited by: Levizzani, V., Kidd, C., Kirschbaum, D. B., Kummerow, C. D., Nakamura, K., and Turk, F. J., Springer International Publishing, Cham, 355–373, https://doi.org/10.1007/978-3-030-24568-9_20, 2020.

Kubota, T., Aonashi, K., Ushio, T., Shige, S., Yamaji, M., Yamamoto, M., Hirose, H., and Takayabu, Y.: A new version of Global Satellite Mapping of Precipitation (GSMaP) product released in December 2021, Copernicus Meetings, https://doi.org/10.5194/egusphere-egu22-3328, 2022.

Kummerow, C., Barnes, W., Kozu, T., Shiue, J., and Simpson, J.: The Tropical Rainfall Measuring Mission (TRMM) Sensor Package, J. Atmospheric Ocean. Technol., 15, 809–817, https://doi.org/10.1175/1520-0426(1998)015%3C0809:TTRMMT%3E2.0.CO;2, 1998.

Kummerow, C. D., Randel, D. L., Kulie, M., Wang, N.-Y., Ferraro, R., Munchak, S. J., and Petkovic, V.: The Evolution of the Goddard Profiling Algorithm to a Fully Parametric Scheme, https://doi.org/10.1175/JTECH-D-15-0039.1, 2015.

Lang, S., Alexe, M., Chantry, M., Dramsch, J., Pinault, F., Raoult, B., Clare, M. C. A., Lessig, C., Maier-Gerber, M., Magnusson, L., Bouallègue, Z. B., Nemesio, A. P., Dueben, P. D., Brown, A., Pappenberger, F., and Rabier, F.: AIFS -- ECMWF's data-driven forecasting system, https://doi.org/10.48550/arXiv.2406.01465, 7 August 2024.

Lavers, D. A., Simmons, A., Vamborg, F., and Rodwell, M. J.: An evaluation of ERA5 precipitation for climate monitoring, Q. J. R. Meteorol. Soc., 148, 3152–3165, https://doi.org/10.1002/qj.4351, 2022.

Lee, M.-I., Schubert, S. D., Suarez, M. J., Held, I. M., Kumar, A., Bell, T. L., Schemm, J.-K. E., Lau, N.-C., Ploshay, J. J., Kim, H.-K., and Yoo, S.-H.: Sensitivity to Horizontal Resolution in the AGCM Simulations of Warm Season Diurnal Cycle of Precipitation over the United States and Northern Mexico, J. Clim., 20, 1862–1881, https://doi.org/10.1175/JCLI4090.1, 2007.

Lewis, E., Fowler, H., Alexander, L., Dunn, R., McClean, F., Barbero, R., Guerreiro, S., Li, X.-F., and Blenkinsop, S.: GSDR: A Global Sub-Daily Rainfall Dataset, J. Clim., 32, 4715–4729, https://doi.org/10.1175/JCLI-D-18-0143.1, 2019.

Li, L., Li, W., and Kushnir, Y.: Variation of the North Atlantic subtropical high western ridge and its implication to Southeastern US summer precipitation, Clim. Dyn., 39, 1401–1412, https://doi.org/10.1007/s00382-011-1214-y, 2012.

Li, P., Li, X.-F., Yu, J., and Yang, S.: Land-Sea Contrast of Global Hourly Precipitation Intensity in ERA5: Dominant Role of Convective Precipitation, Geophys. Res. Lett., 52, e2025GL114733, https://doi.org/10.1029/2025GL114733, 2025.

Light, C. X., Arbic, B. K., Martin, P. E., Brodeau, L., Farrar, J. T., Griffies, S. M., Kirtman, B. P., Laurindo, L. C., Menemenlis, D., Molod, A., Nelson, A. D., Nyadjro, E., O'Rourke, A. K., Shriver, J. F., Siqueira, L., Small, R. J., and Strobach, E.: Effects

https://doi.org/10.5194/egusphere-2026-2867
Preprint. Discussion started: 3 June 2026

of grid spacing on high-frequency precipitation variance in coupled high-resolution global ocean–atmosphere models, Clim. Dyn., 59, 2887–2913, https://doi.org/10.1007/s00382-022-06257-6, 2022.

Lin, Y., Mitchell, K. E., Rogers, E., Baldwin, M. E., and DiMego, G. J.: Test assimilations of the real-time, multi-sensor hourly precipitation analysis into the NCEP Eta model, in: Preprints, 8th Conf. on Mesoscale Meteorology, Boulder, CO, Amer. Meteor. Soc, 341–344, 1999.

Love, B. S., Matthews, A. J., and Lister, G. M. S.: The diurnal cycle of precipitation over the Maritime Continent in a high-resolution atmospheric model, Q. J. R. Meteorol. Soc., 137, 934–947, https://doi.org/10.1002/qj.809, 2011.

Lu, D. and Yong, B.: A Preliminary Assessment of the Gauge-Adjusted Near-Real-Time GSMaP Precipitation Estimate over Mainland China, Remote Sens., 12, 141, https://doi.org/10.3390/rs12010141, 2020.

Lu, J., Li, T., and Wang, L.: Precipitation Diurnal Cycle over the Maritime Continent Modulated by the Climatological Annual Cycle, J. Clim., 34, 1387–1402, https://doi.org/10.1175/JCLI-D-20-0130.1, 2021.

Mega, T. and Ushio, T.: Application of ground observation data in next GSMaP Gauge algorithm, Jpn. Geosci. Union, 2017.

Mega, T., Ushio, T., Takahiro, M., Kubota, T., Kachi, M., and Oki, R.: Gauge-Adjusted Global Satellite Mapping of Precipitation, IEEE Trans. Geosci. Remote Sens., 57, 1928–1935, https://doi.org/10.1109/TGRS.2018.2870199, 2019.

Mesinger, F., DiMego, G., Kalnay, E., Mitchell, K., Shafran, P. C., Ebisuzaki, W., Jović, D., Woollen, J., Rogers, E., Berbery, E. H., Ek, M. B., Fan, Y., Grumbine, R., Higgins, W., Li, H., Lin, Y., Manikin, G., Parrish, D., and Shi, W.: North American Regional Reanalysis, Bull. Am. Meteorol. Soc., 87, 343–360, https://doi.org/10.1175/BAMS-87-3-343, 2006.

Miralles, D. G., Gentine, P., Seneviratne, S. I., and Teuling, A. J.: Land–atmospheric feedbacks during droughts and heatwaves: state of the science and current challenges, Ann. N. Y. Acad. Sci., 1436, 19–35, https://doi.org/10.1111/nyas.13912, 2019.

Molod, A., Takacs, L., Suarez, M., and Bacmeister, J.: Development of the GEOS-5 atmospheric general circulation model: evolution from MERRA to MERRA2, Geosci. Model Dev., 8, 1339–1356, https://doi.org/10.5194/gmd-8-1339-2015, 2015.

Mori, S., Jun-Ichi, H., Tauhid, Y. I., Yamanaka, M. D., Okamoto, N., Murata, F., Sakurai, N., Hashiguchi, H., and Sribimawati, T.: Diurnal Land–Sea Rainfall Peak Migration over Sumatera Island, Indonesian Maritime Continent, Observed by TRMM Satellite and Intensive Rawinsonde Soundings, Mon. Weather Rev., 132, 2021–2039, https://doi.org/10.1175/1520-0493(2004)132%3C2021:DLRPMO%3E2.0.CO;2, 2004.

Ning, S., Song, F., Udmale, P., Jin, J., Thapa, B. R., and Ishidaira, H.: Error Analysis and Evaluation of the Latest GSMap and IMERG Precipitation Products over Eastern China, Adv. Meteorol., 2017, 1803492, https://doi.org/10.1155/2017/1803492, 2017.

Oki, T. and Kanae, S.: Global Hydrological Cycles and World Water Resources, Science, 313, 1068–1072, https://doi.org/10.1126/science.1128845, 2006.

Oppenheim, A. V. and Schafer, R. W.: Discrete-time Signal Processing, Pearson, 1144 pp., 2010.

https://doi.org/10.5194/egusphere-2026-2867
Preprint. Discussion started: 3 June 2026

Osborn, T. J. and Hulme, M.: Development of a Relationship between Station and Grid-Box Rainday Frequencies for Climate Model Evaluation, J. Clim., 10, 1885–1908, https://doi.org/10.1175/1520-0442(1997)010%3C1885:DOARBS%3E2.0.CO;2, 1997.

Parker, M. D. and Ahijevych, D. A.: Convective Episodes in the East-Central United States, Mon. Weather Rev., 135, 3707–3727, https://doi.org/10.1175/2007MWR2098.1, 2007.

Petković, V., Kummerow, C. D., Randel, D. L., Pierce, J. R., and Kodros, J. K.: Improving the Quality of Heavy Precipitation Estimates from Satellite Passive Microwave Rainfall Retrievals, J. Hydrometeorol., 19, 69–85, https://doi.org/10.1175/JHM-D-17-0069.1, 2018.

Pfahl, S. and Wernli, H.: Quantifying the Relevance of Cyclones for Precipitation Extremes, J. Clim., 25, 6770–6780, https://doi.org/10.1175/JCLI-D-11-00705.1, 2012b.

Pradhan, R. K., Markonis, Y., Marra, F., Nikolopoulos, E. I., Papalexiou, S. M., and Levizzani, V.: Diurnal variability of global precipitation: insights from hourly satellite and reanalysis datasets, Hydrol. Earth Syst. Sci., 29, 4929–4949, https://doi.org/10.5194/hess-29-4929-2025, 2025.

Rasmussen, K. L., Zuluaga, M. D., and Houze Jr., R. A.: Severe convection and lightning in subtropical South America, Geophys. Res. Lett., 41, 7359–7366, https://doi.org/10.1002/2014GL061767, 2014.

Rickenbach, T. M., Nieto-Ferreira, R., Zarzar, C., and Nelson, B.: A seasonal and diurnal climatology of precipitation organization in the southeastern United States, Q. J. R. Meteorol. Soc., 141, 1938–1956, https://doi.org/10.1002/qj.2500, 2015.

Rickenbach, T. M., Ferreira, R. N., and Wells, H.: Springtime Onset of Isolated Convection Precipitation across the Southeastern United States: Framework and Regional Evolution, Mon. Weather Rev., 148, 891–906, https://doi.org/10.1175/MWR-D-19-0279.1, 2020.

Shapiro, A., Fedorovich, E., and Rahimi, S.: A Unified Theory for the Great Plains Nocturnal Low-Level Jet, J. Atmospheric Sci., 73, 3037–3057, https://doi.org/10.1175/JAS-D-15-0307.1, 2016.

Skok, G., Žagar, N., Honzak, L., Žabkar, R., Rakovec, J., and Ceglar, A.: Precipitation intercomparison of a set of satellite- and raingauge-derived datasets, ERA Interim reanalysis, and a single WRF regional climate simulation over Europe and the North Atlantic, Theor. Appl. Climatol., 123, 217–232, https://doi.org/10.1007/s00704-014-1350-5, 2016.

Soci, C., Hersbach, H., Simmons, A., Poli, P., Bell, B., Berrisford, P., Horányi, A., Muñoz-Sabater, J., Nicolas, J., Radu, R., Schepers, D., Villaume, S., Haimberger, L., Woollen, J., Buontempo, C., and Thépaut, J.-N.: The ERA5 global reanalysis from 1940 to 2022, Q. J. R. Meteorol. Soc., 150, 4014–4048, https://doi.org/10.1002/qj.4803, 2024.

Song, H., Lin, W., Lin, Y., Wolf, A. B., Neggers, R., Donner, L. J., Del Genio, A. D., and Liu, Y.: Evaluation of Precipitation Simulated by Seven SCMs against the ARM Observations at the SGP Site*, J. Clim., 26, 5467–5492, https://doi.org/10.1175/JCLI-D-12-00263.1, 2013.

Song, J., Song, F., Feng, Z., Leung, L. R., Li, C., and Wu, L.: Realistic Precipitation Diurnal Cycle in Global Convection-Permitting Models by Resolving Mesoscale Convective Systems, Geophys. Res. Lett., 51, e2024GL109945, https://doi.org/10.1029/2024GL109945, 2024.

https://doi.org/10.5194/egusphere-2026-2867
Preprint. Discussion started: 3 June 2026

Song, Y. and Wei, J.: Diurnal cycle of summer precipitation over the North China Plain and associated land–atmosphere interactions: Evaluation of ERA5 and MERRA -2, Int. J. Climatol., 41, 6031–6046, https://doi.org/10.1002/joc.7166, 2021.

Stephens, G. L., L'Ecuyer, T., Forbes, R., Gettelmen, A., Golaz, J.-C., Bodas-Salcedo, A., Suzuki, K., Gabriel, P., and Haynes, J.: Dreary state of precipitation in global models, J. Geophys. Res. Atmospheres, 115, https://doi.org/10.1029/2010JD014532, 2010.

Stirling, A. J. and Stratton, R. A.: Entrainment processes in the diurnal cycle of deep convection over land, Q. J. R. Meteorol. Soc., 138, 1135–1149, https://doi.org/10.1002/qj.1868, 2012.

Sun, Q., Miao, C., Duan, Q., Ashouri, H., Sorooshian, S., and Hsu, K.: A Review of Global Precipitation Data Sets: Data Sources, Estimation, and Intercomparisons, Rev. Geophys., 56, 79–107, https://doi.org/10.1002/2017RG000574, 2018.

Tang, S., Xie, S., Zhang, M., Tang, Q., Zhang, Y., Klein, S. A., Cook, D. R., and Sullivan, R. C.: Differences in Eddy-Correlation and Energy-Balance Surface Turbulent Heat Flux Measurements and Their Impacts on the Large-Scale Forcing Fields at the ARM SGP Site, J. Geophys. Res. Atmospheres, 124, 3301–3318, https://doi.org/10.1029/2018JD029689, 2019.

Tang, S., Gleckler, P., Xie, S., Lee, J., Ahn, M.-S., Covey, C., and Zhang, C.: Evaluating the Diurnal and Semidiurnal Cycle of Precipitation in CMIP6 Models Using Satellite- and Ground-Based Observations, J. Clim., 34, 3189–3210, https://doi.org/10.1175/JCLI-D-20-0639.1, 2021.

Tao, C., Xie, S., Ma, H., Bechtold, P., Cui, Z., Vaillancourt, P. A., Van Weverberg, K., Wang, Y., Wong, M., Yang, J., Zhang, G. J., Choi, I., Tang, S., Wei, J., Wu, W., Zhang, M., Neelin, J. D., and Zeng, X.: Diurnal cycle of precipitation over the tropics and central United States: intercomparison of general circulation models, Q. J. R. Meteorol. Soc., 150, 911–936, https://doi.org/10.1002/qj.4629, 2024.

Tashima, T., Kubota, T., Mega, T., and Shige, S.: Improvement of the GSMaP Precipitation Retrieval Algorithm for Microwave Sounders Over Coast, in: 2021 IEEE International Geoscience and Remote Sensing Symposium IGARSS, 2021 IEEE International Geoscience and Remote Sensing Symposium IGARSS, 832–835, https://doi.org/10.1109/IGARSS47720.2021.9553633, 2021.

Tian, Y. and Kuang, Z.: Dependence of entrainment in shallow cumulus convection on vertical velocity and distance to cloud edge, Geophys. Res. Lett., 43, 4056–4065, https://doi.org/10.1002/2016GL069005, 2016.

Trenberth, K. E., Dai, A., Rasmussen, R. M., and Parsons, D. B.: The Changing Character of Precipitation, Bull. Am. Meteorol. Soc., 84, 1205–1218, https://doi.org/10.1175/BAMS-84-9-1205, 2003b.

Tustison, B., Harris, D., and Foufoula-Georgiou, E.: Scale issues in verification of precipitation forecasts, J. Geophys. Res. Atmospheres, 106, 11775–11784, https://doi.org/10.1029/2001JD900066, 2001.

Ushio, T., Sasashige, K., Kubota, T., Shige, S., Okamoto, K., Aonashi, K., Inoue, T., Takahashi, N., Iguchi, T., Kachi, M., Oki, R., Morimoto, T., and Kawasaki, Z.-I.: A Kalman Filter Approach to the Global Satellite Mapping of Precipitation (GSMaP) from Combined Passive Microwave and Infrared Radiometric Data, J. Meteorol. Soc. Jpn. Ser II, 87A, 137–151, https://doi.org/10.2151/jmsj.87A.137, 2009.

https://doi.org/10.5194/egusphere-2026-2867
Preprint. Discussion started: 3 June 2026

Wang, B. and Ding, Q.: Global monsoon: Dominant mode of annual variation in the tropics, Dyn. Atmospheres Oceans, 44, 165–183, https://doi.org/10.1016/j.dynatmoce.2007.05.002, 2008.

Wang, B., Liu, J., Kim, H.-J., Webster, P. J., and Yim, S.-Y.: Recent change of the global monsoon precipitation (1979–2008), Clim. Dyn., 39, 1123–1135, https://doi.org/10.1007/s00382-011-1266-z, 2012.

Watters, D., Battaglia, A., and Allan, R. P.: The Diurnal Cycle of Precipitation according to Multiple Decades of Global Satellite Observations, Three CMIP6 Models, and the ECMWF Reanalysis, J. Clim., 34, 5063–5080, https://doi.org/10.1175/JCLI-D-20-0966.1, 2021.

Wu, W.-S., Purser, R. J., and Parrish, D. F.: Three-Dimensional Variational Analysis with Spatially Inhomogeneous Covariances, Mon. Weather Rev., 130, 2905–2916, https://doi.org/10.1175/1520-0493(2002)130%3C2905:TDVAWS%3E2.0.CO;2, 2002.

Xie, P. and Arkin, P. A.: Global Precipitation: A 17-Year Monthly Analysis Based on Gauge Observations, Satellite Estimates, and Numerical Model Outputs, Bull. Am. Meteorol. Soc., 78, 2539–2558, https://doi.org/10.1175/1520-0477(1997)078%3C2539:GPAYMA%3E2.0.CO;2, 1997.

Xie, P., Chen, M., Yang, S., Yatagai, A., Hayasaka, T., Fukushima, Y., and Liu, C.: A Gauge-Based Analysis of Daily Precipitation over East Asia, J. Hydrometeorol., 8, 607–626, https://doi.org/10.1175/JHM583.1, 2007.

Xie, P., Joyce, R., Wu, S., Yoo, S.-H., Yarosh, Y., Sun, F., and Lin, R.: Reprocessed, Bias-Corrected CMORPH Global High-Resolution Precipitation Estimates from 1998, J. Hydrometeorol., 18, 1617–1641, https://doi.org/10.1175/JHM-D-16-0168.1, 2017.

Xie, S. and Zhang, M.: Impact of the convection triggering function on single-column model simulations, J. Geophys. Res. Atmospheres, 105, 14983–14996, https://doi.org/10.1029/2000JD900170, 2000.

Yamamoto, M. K. and Kubota, T.: Implementation of a Rainfall Normalization Module for GSMaP Microwave Imagers and Sounders, Remote Sens., 14, 4445, https://doi.org/10.3390/rs14184445, 2022.

Yang, B., Wang, M., Zhang, G. J., Guo, Z., Huang, A., Zhang, Y., and Qian, Y.: Linking Deep and Shallow Convective Mass Fluxes via an Assumed Entrainment Distribution in CAM5-CLUBB: Parameterization and Simulated Precipitation Variability, J. Adv. Model. Earth Syst., 13, e2020MS002357, https://doi.org/10.1029/2020MS002357, 2021.

Yang, G.-Y. and Slingo, J.: The Diurnal Cycle in the Tropics, Mon. Weather Rev., 129, 784–801, https://doi.org/10.1175/1520-0493(2001)129%3C0784:TDCITT%3E2.0.CO;2, 2001.

Yong, B., Chen, B., Gourley, J. J., Ren, L., Hong, Y., Chen, X., Wang, W., Chen, S., and Gong, L.: Intercomparison of the Version-6 and Version-7 TMPA precipitation products over high and low latitudes basins with independent gauge networks: Is the newer version better in both real-time and post-real-time analysis for water resources and hydrologic extremes?, J. Hydrol., 508, 77–87, https://doi.org/10.1016/j.jhydrol.2013.10.050, 2014.

Yu, R., Zhou, T., Xiong, A., Zhu, Y., and Li, J.: Diurnal variations of summer precipitation over contiguous China, Geophys. Res. Lett., 34, https://doi.org/10.1029/2006GL028129, 2007.

Zhang, C.: Madden-Julian Oscillation, Rev. Geophys., 43, https://doi.org/10.1029/2004RG000158, 2005.

https://doi.org/10.5194/egusphere-2026-2867
Preprint. Discussion started: 3 June 2026

Zhang, M. H., Lin, J. L., Cederwall, R. T., Yio, J. J., and Xie, S. C.: Objective Analysis of ARM IOP Data: Method and Sensitivity, Mon. Weather Rev., 129, 295–311, https://doi.org/10.1175/1520-0493(2001)129%3C0295:OAOAID%3E2.0.CO;2, 2001.

Zhao, Y., Huang, A., Zhou, Y., Huang, D., Yang, Q., Ma, Y., Li, M., and Wei, G.: Impact of the Middle and Upper Tropospheric Cooling over Central Asia on the Summer Rainfall in the Tarim Basin, China, J. Clim., 27, 4721–4732, https://doi.org/10.1175/JCLI-D-13-00456.1, 2014b.

Zscheischler, J., Martius, O., Westra, S., Bevacqua, E., Raymond, C., Horton, R. M., Van Den Hurk, B., AghaKouchak, A., Jézéquel, A., Mahecha, M. D., Maraun, D., Ramos, A. M., Ridder, N. N., Thiery, W., and Vignotto, E.: A typology of compound weather and climate events, Nat. Rev. Earth Environ., 1, 333–347, https://doi.org/10.1038/s43017-020-0060-z, 2020.